UCRL-18088

cy. 2

POLARIZATION IN PROTON-HELIUM SCATTERING AT 70 AND 80 MeV

Albert W. Stetz

(Ph. D. Thesis)

December 1968

LAWRENCE RADIATION LABORATORY
UNIVERSITY of CALIFORNIA BERKELEY

UCRL-18088

cy. 2

DISCLAIMER

UCRL-18088

UNIVERSITY OF CALIFORNIA
Lawrence Radiation Laboratory
Berkeley, California

AEC Contract No. W-7405-eng-48

POLARIZATION IN PROTON-HELIUM SCATTERING AT 70 AND 80 MeV

Albert W. Stetz

(Ph. D. Thesis)

December 1968

I. INTRODUCTION

A. Proton-Helium Interaction

Recent interest in the interaction of protons with helium nuclei dates back to the experiment of Freier, Lampi, Sleater, and Williams,[1] and the analysis of Critchfield and Dodder[2] in 1949. Critchfield and Dodder carried out a phase shift analysis of the differential cross section data at energies ranging from 0.95 MeV to 3.58 MeV. They found two phase shift solutions which fitted the data adequately. One solution predicted a ground state of Li^5 with quantum numbers $p_{1/2}$ followed by an excited state with spin 3/2 (i.e., a normal doublet in Li^5). The other solution predicted an inverted ordering of these levels. It was impossible to decide between these two solutions on the basis of differential cross sections alone; however, the predicted polarizations differed widely in the two cases, and the single polarization measurement by Heusinkveld and Freir[3] decided in favor of the inverted doublet arrangement.

By 1957 the region between 0 and 17 MeV had been thoroughly explored experimentally and various analyses undertaken. This work was largely motivated by the following two considerations:

First, proton-helium scattering manifests strong polarization over the entire range of energies investigated. This makes it a convenient analyzer for polarized protons as well as a source of polarized proton beams.

Second, the proton-helium system is the simplest nuclear system with a tightly bound, spin-zero target. There is no opportunity for nuclear break up below the $p + He^4 \rightarrow d + He^3$ threshold at 22.9 MeV. Analysis is further simplified by the fact that parity forbids the mixing of scattering states with different orbital angular momenta. This has made the proton-helium interaction an important proving ground for phenomeno-

logical theories of nuclear reactions. For example, potential-well analyses of the phase shifts have been given by Sack, Biedeharn, and Breit,[4] and by Gammel and Thaler.[5] Adair,[6] Dodder and Gammel,[7] and Miller and Phillips[8] have given nuclear dispersion theory analyses. Finally, Herzenenberg and Squires[9] tried to interpret the differential cross section data in terms of the collective effects of the individual nucleons interacting according to a simple nucleon-nucleon potential. In each instance the calculations confirmed the ordering of the levels of Li^5 and yielded quantitative agreement with the available data, but were unsuccessful in predicting the polarization at other energies.[10]

Part of the difficulty of the older calculations in predicting experimental results above 20 MeV was due to their neglect of inelasticity. As higher energy data became available, first at 40 MeV and later at 48 and 29 MeV, various phase shift calculations were attempted which took inelasticity into account by employing complex phase shifts. The first such analyses of the 40 MeV data were published by Suwa and Yokosawa,[11] and Giamati, Madsen, and Thaler.[12] The two solutions gave comparable agreement with both differential cross section and polarization data, but disagreed with each other even on the qualitative behavior of the phase shifts. The dilemma was eventually resolved in favor of the Suwa and Yokosawa solution by a measurement of the spin rotation parameter[13] and small angle polarization.[14]

Since this difficulty was resolved, subsequent phase shift solutions[13,15] of new data at 28, 31, 49, 55, and 63 MeV have fallen in line with the Suwa-Yokosawa result and the earlier work below 18 MeV. The details of these analyses will be discussed in a later section. Data is available at only a few scattered energies above 63 MeV. It would be

hopeless to extend the phase shift analysis beyond this point without further experimental work in the region between 63 and 90 MeV, the next energy at which data exists.

B. Helium-Filled Streamer Chambers

A recent development in the field of nuclear instrumentation has given new impetus to the study of proton-helium scattering. It was discovered by Fukui and Miyamoto[16] in 1958 that electrical discharges in noble gases could be used to delineate the paths of charged particles. The basic mechanism is as follows: When a charged particle passes through gas it leaves behind it a path of ion pairs. If a strong electrical field is applied before the ions can recombine, the free electrons will be accelerated and undergo further ionizing collisions. In this way the number of free electrons in the vicinity of the original ions will grow exponentially. If the field is of the order of 20 to 30 kV/cm there will be enough ion pairs localized within a few millimeters of the original path of the ionizing particle to produce, upon recombination, enough light to photograph. A device which uses electron multiplication in this way to detect the passage of a charged particle is usually called a "streamer chamber." It offers important advantages over conventional spark chambers because of its spatial isotropy and its ability to resolve many-particle events. Unlike a bubble chamber it may be triggered by fast electronics in such a way as to select those events in which the experimenter is interested.

Early streamer chamber development concentrated on neon gas because of its low ionization potential and convenient spectrum. One can take advantage of the analyzing power of helium, however, to do polarization experiments with streamer chambers in an especially convenient way.

The experiment is arranged so that the nucleons to be analyzed rescatter from the helium in the active volume of the chamber. The left-right asymmetry of these events is observed, and this yields the nucleon polarization once the analyzing power of helium is known. This technique can be used to study the polarization of neutrons and very low energy protons where polarized target and conventional double-scattering methods are impracticable. It is of obvious importance in the study of nucleon polarization in the reactions $\pi^- p \rightarrow \pi^0 n$, and $\pi^- p \rightarrow \pi^- p$ in the forward direction.

In spite of its advantages, the helium-filled streamer chamber still did not seem to be a practical tool for these experiments. There were two reasons why: First, it is far more difficult to obtain reliable streamer formation in helium than in neon. Second, the analyzing power of helium is known only up to 60 MeV. With this in mind we decided to do a streamer chamber experiment aimed first at solving the practical problems of obtaining reliable streamer chamber operation, and second, at extending our knowledge of the proton-helium interaction into the unexplored region above 60 MeV.

II. EXPERIMENTAL METHOD AND APPARATUS

A. General

A measurement of the analyzing power of a target particle involves detecting an azimuthal asymmetry in the scattering of a previously polarized beam. The analyzing power $A(\theta)$ is then obtained from the equation

$$a(\theta,\phi) = P_o A(\theta)|\cos\phi|,$$

where θ is the polar scattering angle, ϕ is the angle between the plane of the first scatter and the plane of the second (see Fig. 1), P_o is the incident beam polarization, and $a(\theta,\phi)$ is the left-right asymmetry observed at the angles θ and ϕ. It follows from the invariance of strong interactions under time reversal that the analyzing power defined in this way is equal to the polarization the target particle would induce in a previously unpolarized beam. For this reason the words "polarization" and "analyzing power" will be used interchangeably.

In previous experiments measuring the analyzing power of helium, counter systems were used to compare counting rates at $\cos\phi = +1$ and $\cos\phi = -1$ for various values of θ. At energies where inelastic reactions are prevalent, however, it is difficult to distinguish elastic events on the basis of counter data alone. In this case it is preferable to use a visual detector which, in addition to sampling a wide range of θ and ϕ, yields enough kinematic information to constrain the event.

In this experiment a helium-filled streamer chamber was used as the target as well as the detector. This enabled us to measure the scattering angle of the proton as well as the recoil helium nucleus. Moreover, any events in which three or more charged particles appeared in the final state could be immediately recognized and rejected.

The resulting experimental set up is shown in Fig. 2. The polarized

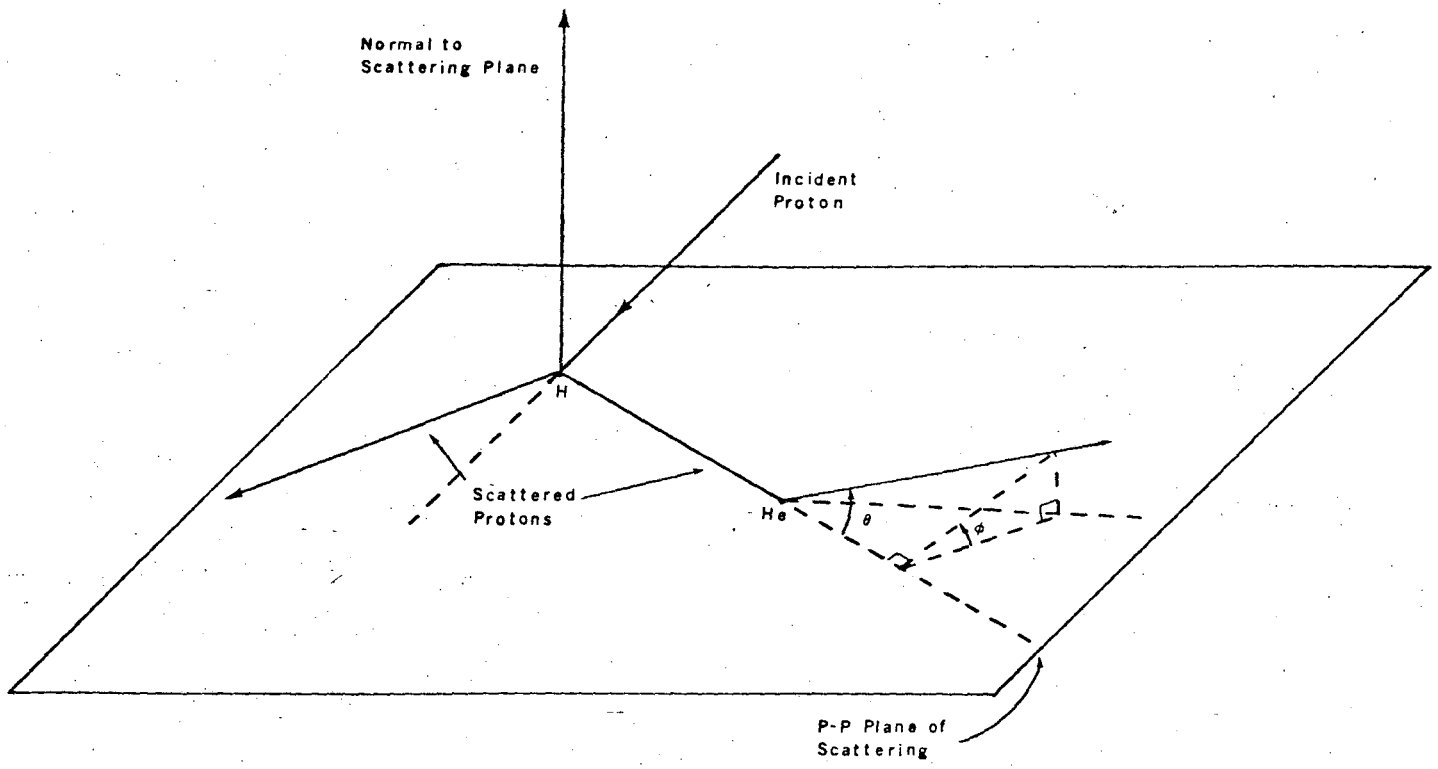

XBL 685-819

Fig. 1. A proton-proton scattering event followed by a second scatter from helium. This diagram defines the angles θ and ϕ used in the $p + He^4$ scattering analysis.

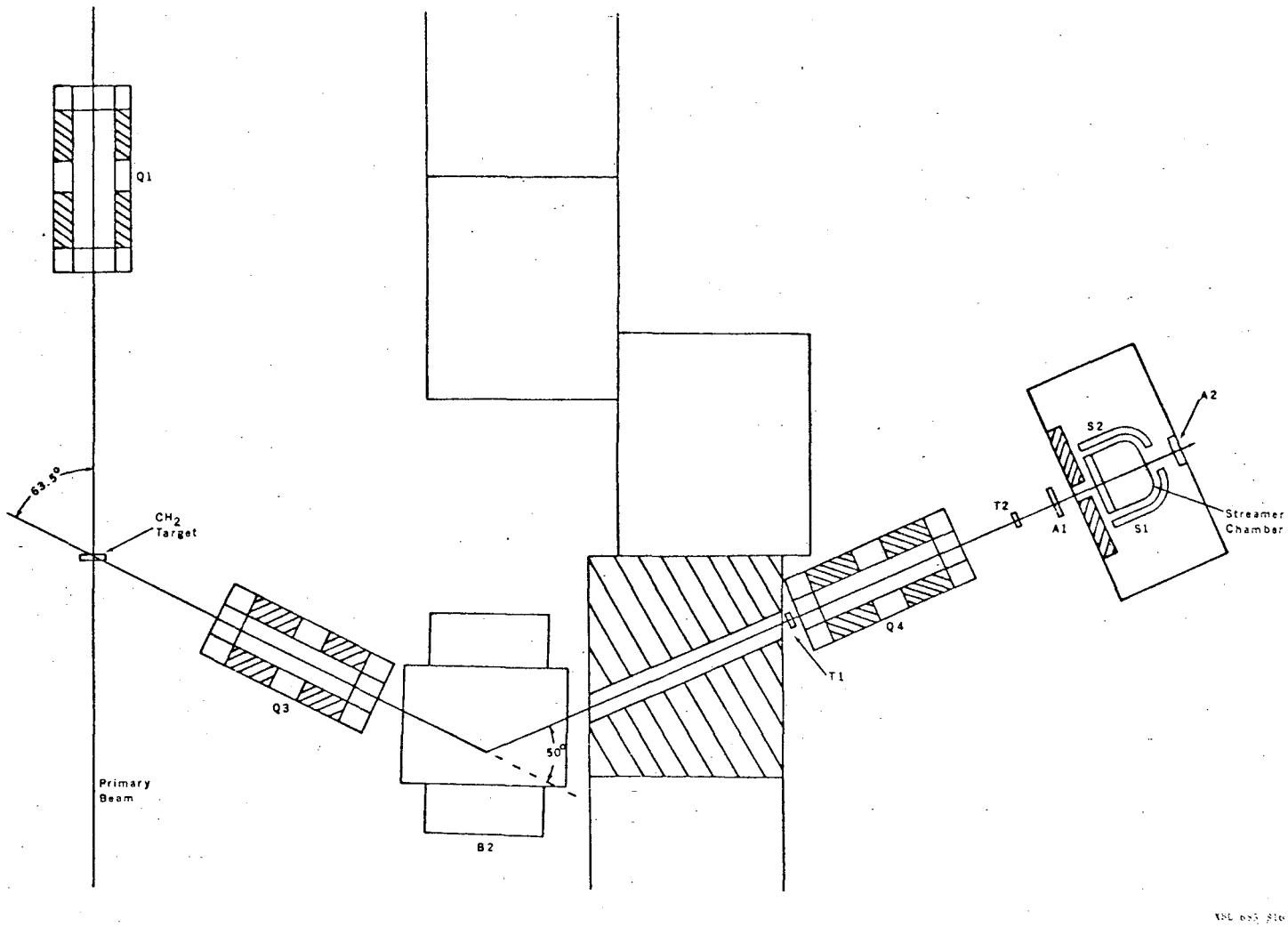

Fig. 2. Experimental layout of the beam, counters, and streamer chamber.

beam is produced by scattering from protons in polyethylene. This beam is momentum analyzed and focussed to a small image at the position of the streamer chamber. The chamber is surrounded by a belt of counters so that protons scattering from helium nuclei can, if their plane of scattering is nearly horizontal, pass through one of the counters and trigger the system.

The streamer chamber was pulsed and photographed after each trigger event. Only one view of the chamber, that looking perpendicularly to the plane of scattering, was recorded. In addition to the actual tracks of the particles, a configuration of data lights appeared on each frame denoting whether the right or left side counter was struck by the recoiling proton. With this information the left-right scattering asymmetry was obtained directly as a function of the laboratory scattering angle.

B. The Beam

The 184-inch cyclotron produces an external proton beam of 735 ± 20 MeV energy. This beam was focused by the quadrupole triplet Q2, as shown in Fig. 2, to obtain a small spot at the target. The target was a 5 x 2 x 1/2-in. block of polyethylene with the chemical composition CH_2. The low energy polarized protons were the result of elastic scattering from hydrogen at a lab angle of 63.5 deg. At this angle the recoil protons have an energy of 100 MeV and a polarization[18] of -56 ± 3%.

In addition to the protons scattered elastically, a small fraction were scattered inelastically at the same angle and with the same energy from carbon nuclei. The flux and polarization of these protons were determined by comparing the counting rates and asymmetries due to the polyethylene target with those resulting from a pure carbon target.

The recoil protons were focused and momentum analyzed by the quadrupole doublets Q3 and Q4 and the bending magnet B2. The beam optics are shown in Fig. 3. The slit in front of Q3 limits its angular acceptance to reduce the flux of inelastically scattered protons. In order to achieve the maximum momentum resolution at the given bending angle and beam length, the target was oriented so that its width as seen from Q3, and consequently its image at the first focal point, was as narrow as possible. The second slit, which was located at the first focal point in the horizontal plane, selects the desired range of momenta, 450 ± 10 MeV/c. The second quadrupole Q4 focused an image of this slit about two inches high by one inch wide at the streamer chamber. Helium bags were used between the target and the chamber to reduce multiple scattering.

The currents in the three magnets were initially calculated with the help of the computer program OPTIK.[19] These calculations were checked first with

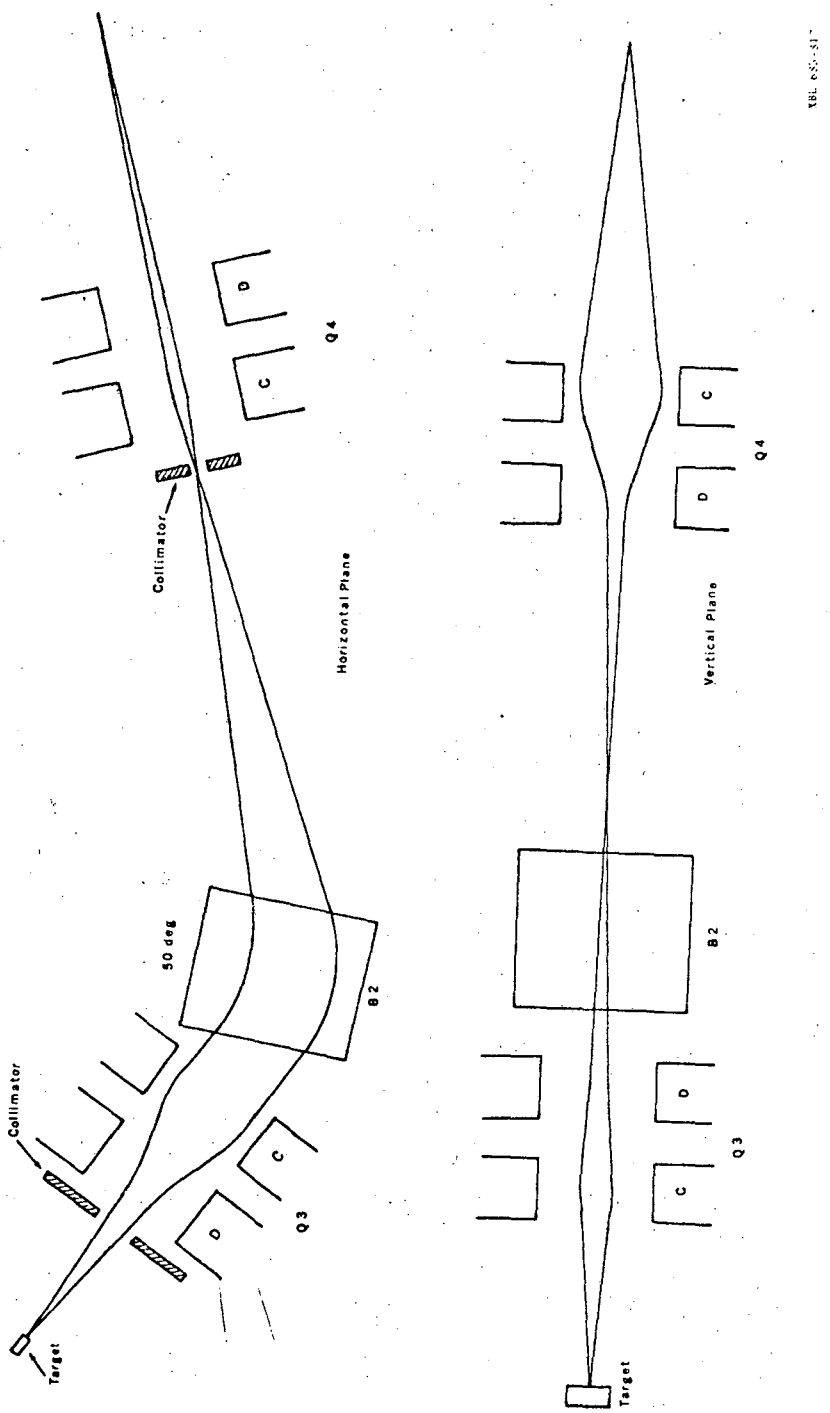

Fig. 3. Beam optics for the polarized proton beam.

the magnetically suspended wire orbit technique, and later by plotting a range curve. Finally, the currents in Q4 were adjusted to obtain the optimum beam profile at the streamer chamber.

After being degraded by passing through the target, the long beam path, and several counters, the final beam energy was 80 ± 2 MeV. For the 70 MeV runs an extra 1.5 inches of polyethylene absorber was placed in the beam at the first focal point. The integral range curves for the 70 and 80 MeV beams are shown in Fig. 4.

The beam was monitored by a set of three counters as shown in Fig. 5a. Protons were identified by their time of flight between counters T1 and T2. A1 is an anti-counter with a hole just large enough to pass the properly focused portion of the beam. In addition to monitoring the beam profile, this counter reduced the probability of the chamber being triggered by protons sprayed out of the beam channel.

The maximum flux obtainable was about 10^5 protons/sec. Normally the intensity of the primary beam was reduced to provide 2×10^4 protons/sec at the streamer chamber. This was the maximum flux that could be tolerated since the unscattered beam tracks tended to obscure the scattering vertices.

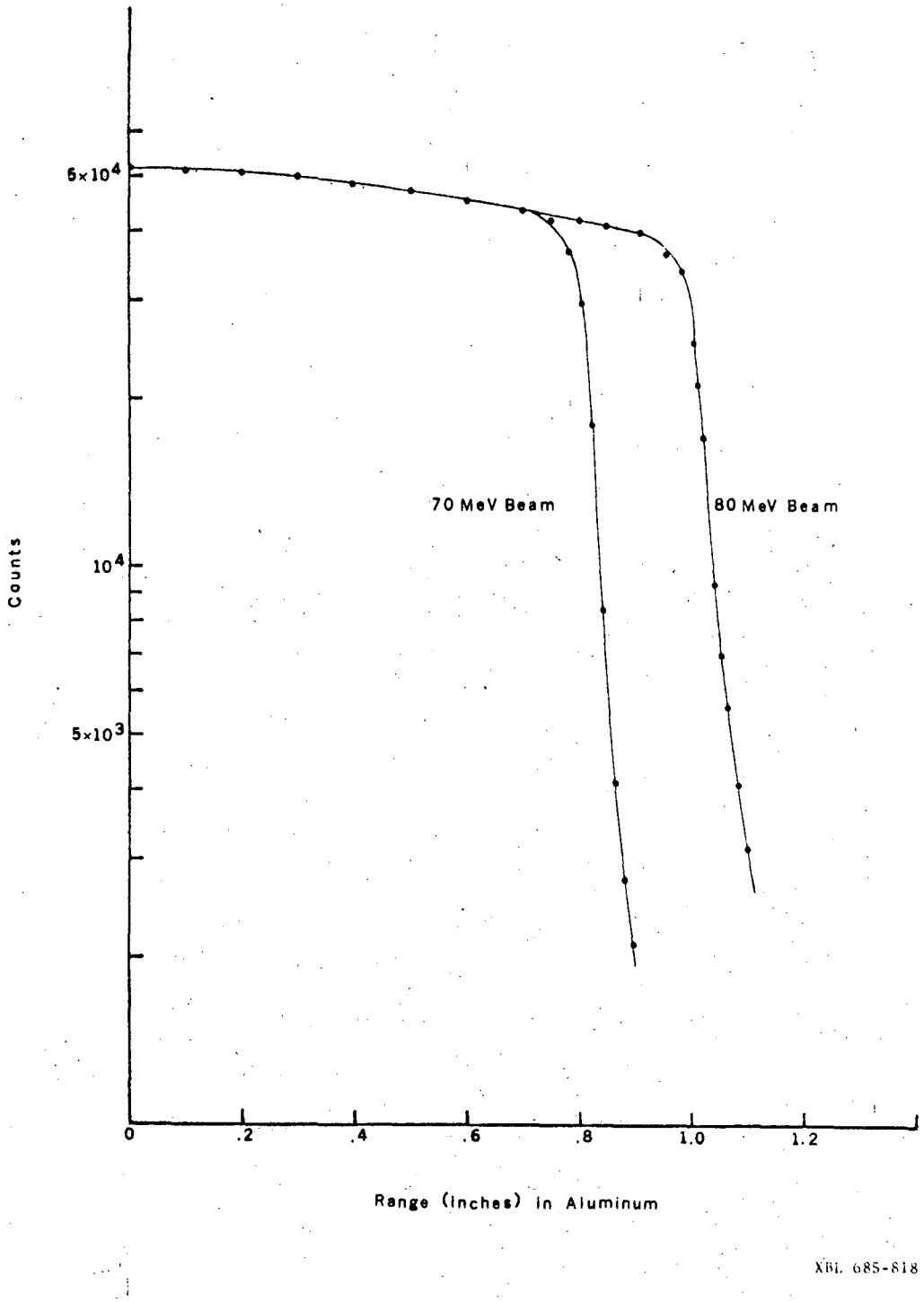

Fig. 4. Integral beam range in aluminum.

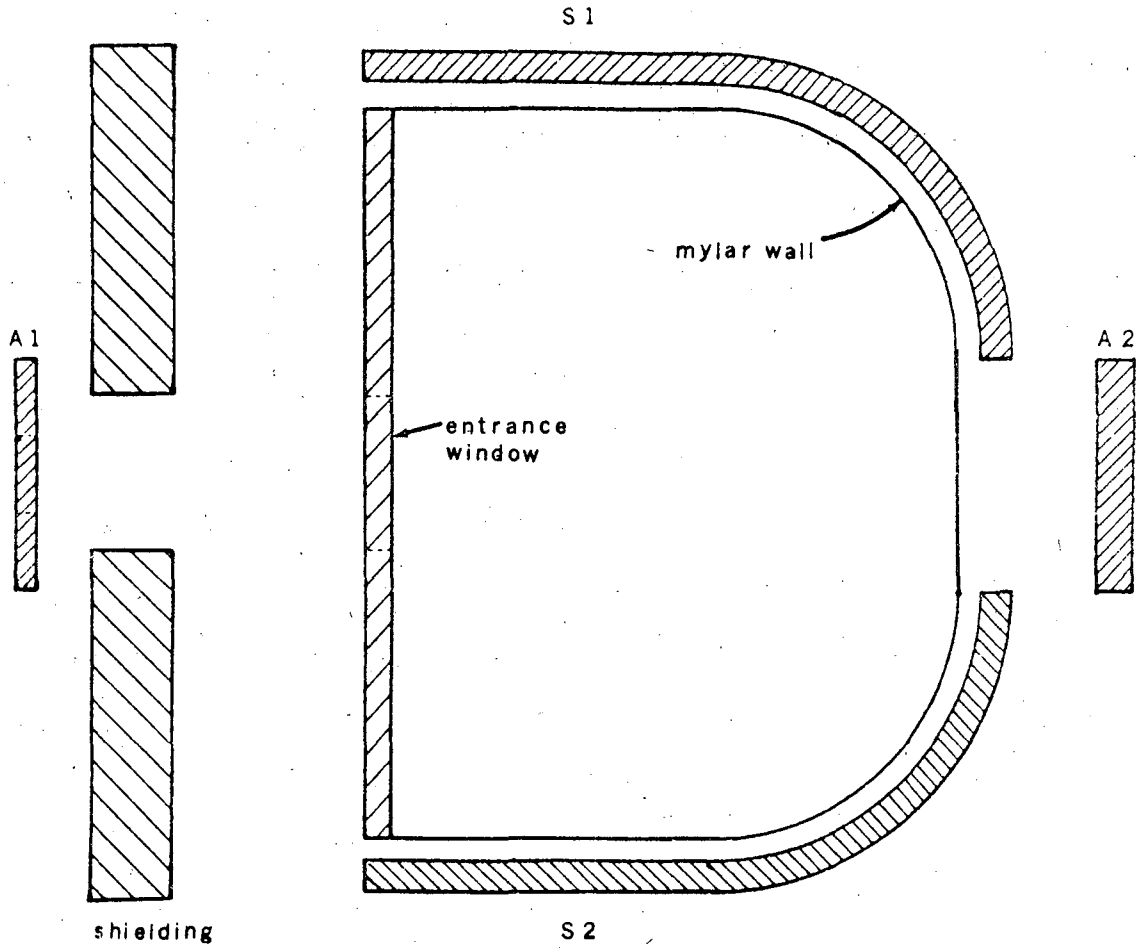

(b) Streamer chamber and surrounding counters.

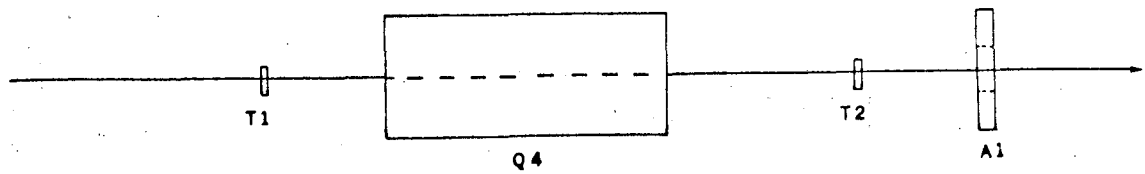

XBL 688-5646

Fig. 5. (a) Final quadrupole and beam counter.

C. Counters and Electronics

The arrangement of scintillation counters in the beam and around the streamer chamber is shown in Figs. 5. (a) and (b). Counters T1 and T2, which were used to obtain the time-of-flight information for the incident particle, were made of "Pilot-B" scintillation material coupled to RCA type 56 AVP photomultiplier tubes with short light pipes. The sensitive area of T2 was made 1/32-in. thick to reduce multiple scattering. The anode signals from the two photomultipliers were differentiated to improve timing accuracy, and each dynode signal was used to set the threshold of a tunnel-diode discriminator so that it fired near the beginning of the positive portion of the differentiated anode signal. This technique[21] greatly reduces the time slewing of the discriminator due to amplitude fluctuations of the photomultiplier output.

The performance of the system was checked and monitored with a Chronetics time-to-height converter and a pulse height analyzer. (See Fig. 6. (a)). The timing resolution was 1 nsec full width at half height.

The difference in times required for a 400 MeV/c proton and a pion of the same momentum to traverse the distance between T1 and T2 was 8.4 nsec. Thus it was possible to avoid triggering the system on pions by making the net resolving time of the discriminator-coincidence circuitry less than 8.4 nsec. The necessary timing and shaping of the discriminator pulses are illustrated in Fig. 6. (b).

In order to trigger the chamber, a coincidence was required between T1 and T2 together with S1 or S2. A signal arriving from either A1 or A2 within 25 nsec would veto the decision (see Fig. 7). This feature reduced the number of spurious triggers due to beam spray and back scattering of beam particles. A separate coincidence was required between either S1 or

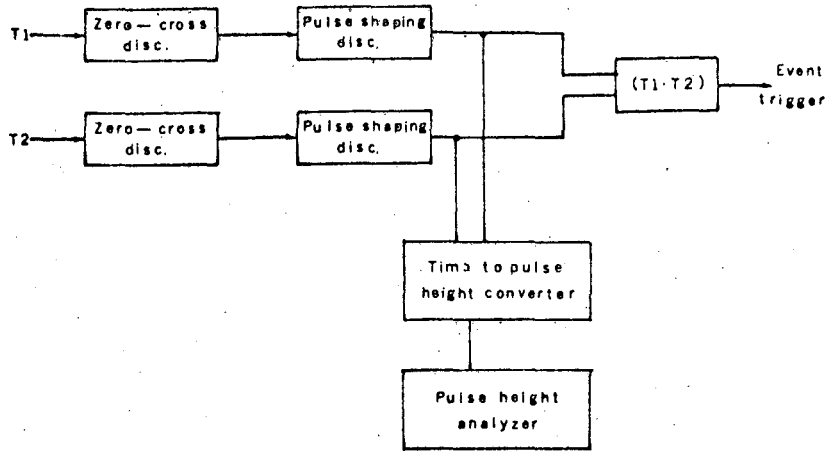

Fig. 6. (a) Simplified logic for the time-of-flight measurement.

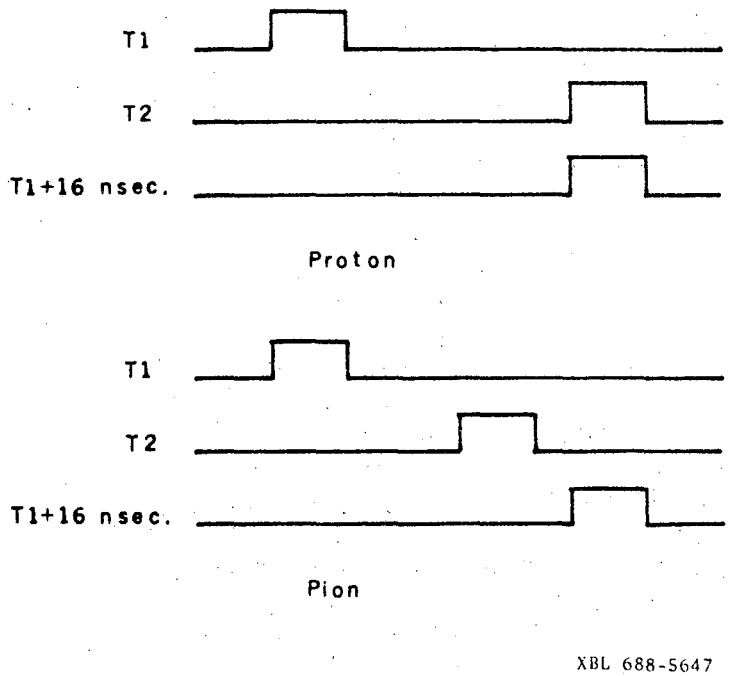

(b) Timing of discriminator pulses for protons and pions.

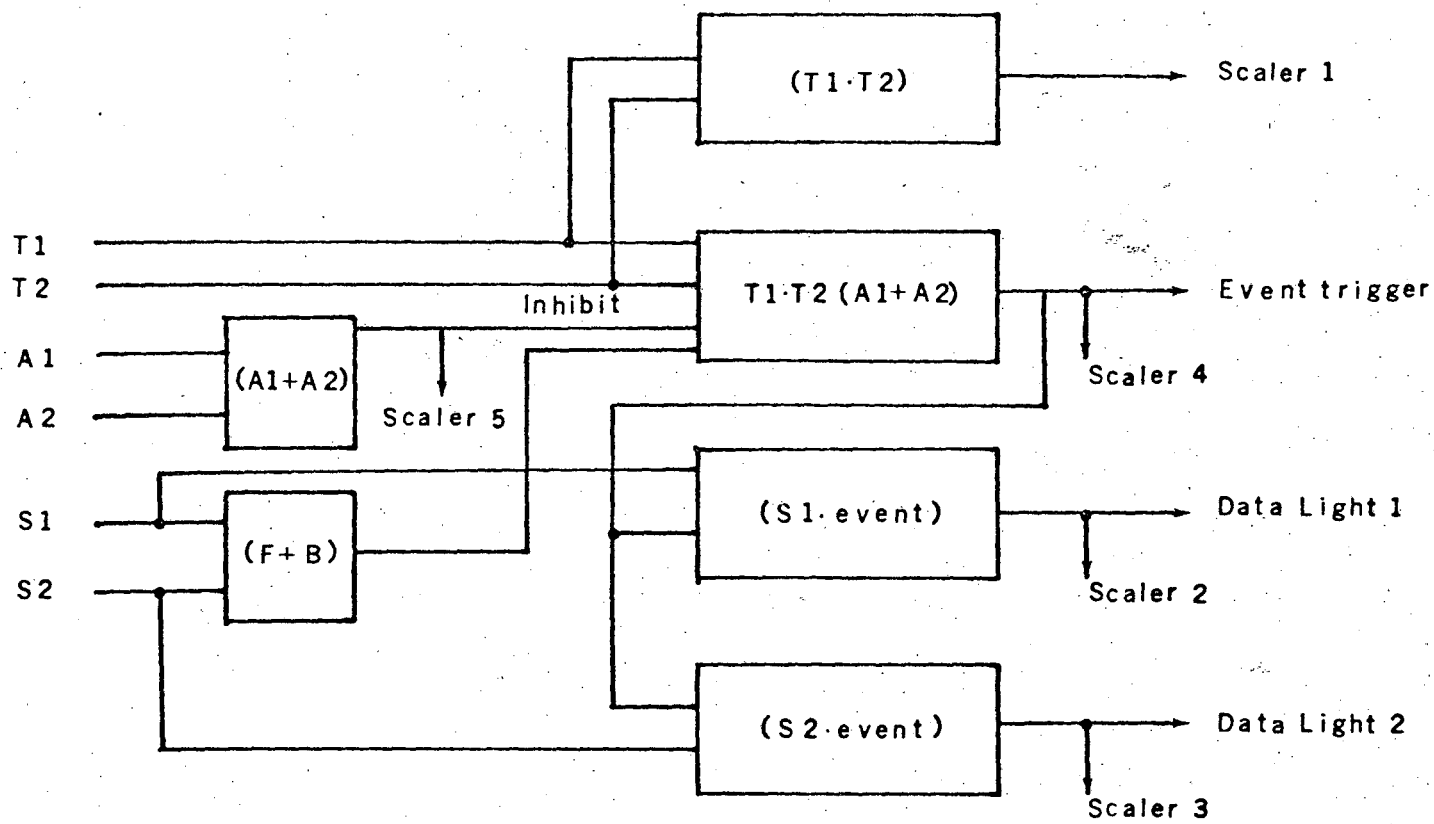

XBL 685-813

Fig. 7. Simplified logic diagram showing the coincidences required to trigger the chamber and light the data lights.

S2 and the event trigger. The output signal from this coincidence was used to light either one of two data lights depending on whether the proton that triggered the system scattered to the right (S1) or to the left (S2).

D. The Streamer Chamber System

1. The Marx Generator

In order to obtain streamer formation in helium with adequate spatial resolution and luminosity,[22] electric fields on the order of 20 to 30 kV/cm are required for a period of time of from 5 to 15 nsec. (See Appendix A.) Either a d.c. high-voltage power supply or an autotransformer might make a practicable power source for streamer chamber operation, but the Marx generator was chosen because of its relatively low cost and reliable operation.

The Marx generator, shown schematically in Fig. 8, is essentially a bank of capacitors charged in parallel and switched in series with fast spark gaps. Initially, each capacitor is charged to voltage V_0, and each gap must sustain this voltage without sparking. To trigger the discharge, the first gap is overvoltaged from a third electrode. When this gap has become conductive, the voltage on the first capacitor is divided among the n-1 remaining gaps so that the second gap is overvoltaged by an amount $V_0/(n-1)$. The transit time required by a pulse to propagate along the system is negligible, so the remaining gaps break down essentially simultaneously under the influence of the initial overvoltage.

The physical layout of the generator built for this experiment is shown in Fig. 9. Each of its seven stages consists of four $BaTiO_2$ capacitors with a net (nominal) capacitance of 3900 pf and 60 kV maximum working voltage. The switching gaps are 0.5-in. brass balls operated in nitrogen. The capacitors and gaps are mounted between two parallel uprights with the 47 kΩ charging resistors mounted on the sides. The entire assembly was made as compact as possible to minimize stray inductance and is mounted in a pressurized tank to eliminate arcing among the high voltage components.

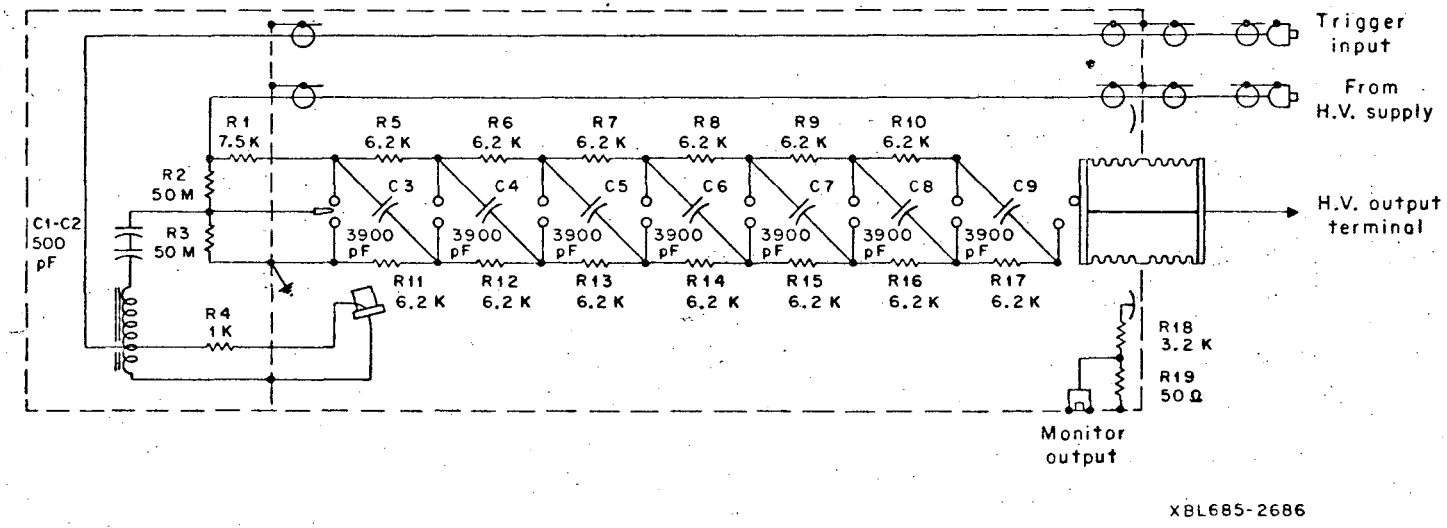

Fig. 8. Circuit of seven-stage 350-kV Marx generator.

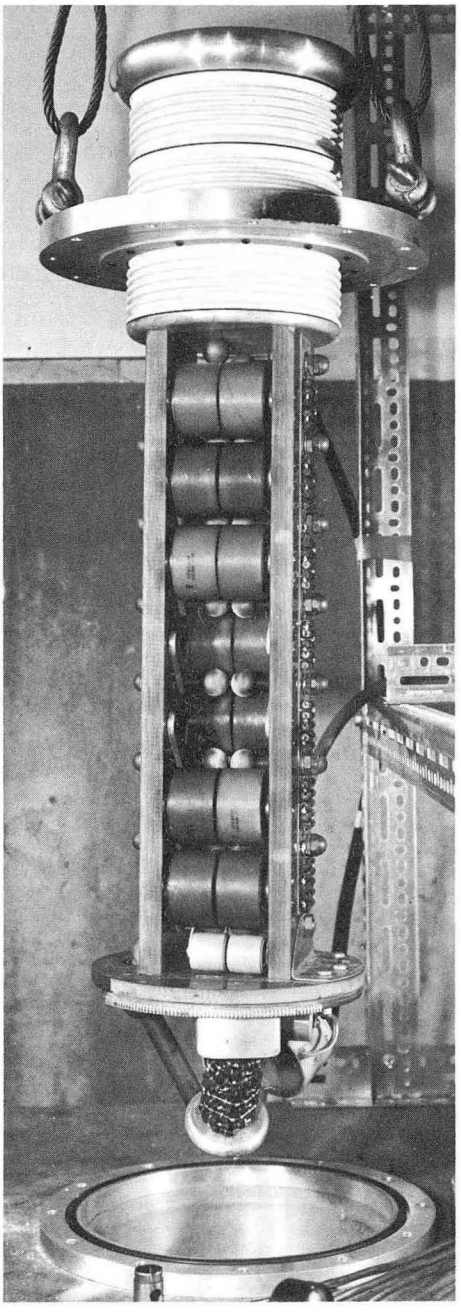

GPR-3142

Fig. 9. Layout of Marx generator with several capacitors removed to show spark gaps.

During the experiment the generator was operated at 48 kV input voltage with gap spacing of 0.1-in. and 100 lbs/in.^{2} pressure. The output was 300 kV with a 10 nanosecond risetime into a 100 Ω load.

2. Transmission Line and Chamber Assembly

If the output of the Marx generator were applied directly to the chamber, streamers would continue to spread during the long tail of the high voltage pulse. For this reason a parallel spark gap was connected across the output of the generator to short-circuit the chamber after some predetermined spark formation time. This gap consisted of 2-in.-brass electrodes operated in dry nitrogen pressurized about two atmospheres. No attempt was made to trigger this gap, but a source of ultraviolet light was flashed at the anode to liberate photoelectrons. These electrons essentially eliminated the time jitter in the interval between the arrival of the high voltage pulse and the formation of a spark. The width of the pulse, and consequently the length and luminosity of the streamers, was controlled by changing the gap pressure and spacing. The final result of the Marx generator and shorting gap was a roughly triangular pulse with a 10 nsec rise time and 5 nsec fall time.

With pulses as short as 10 nsec some care must be taken to operate the chamber as part of a properly matched and terminated transmission line, otherwise the capacitance and inductance of the system will conspire to distort the high voltage pulse and produce nonuniformities in streamer development across the chamber. Generally speaking the configuration of two long parallel conducting strips (like a streamer chamber) behaves like a transmission line of impedance

$$Z_o = 377 \text{ (spacing/width)} \text{ ohms},$$

whereas the Marx generator is a much higher impedance source. Therefore, one must be careful to flare the transmission line gradually from the source

to the chamber in order to transfer as much energy as possible without distorting the pulse shape.

The layout used in the experiment is shown in Fig. 10. The output of the Marx generator was flared out to a strip line 24-in. wide with 5.5-in. electrode spacing. The parallel spark gap was placed between the high voltage electrode and the ground plane at the point where the line begins to flare. The line is terminated in 100 Ω near the downstream end. Three 300 Ω resistors made with $CuSO_4$ electroyte and copper electrodes provided the termination resistance.

The chamber was photographed through a window in the high-voltage side of the transmission line. The window was covered with a fine mesh of expanded metal, which was almost 100% transparent while still electrically conductive.

It is important to have some means of monitoring the shape of the pulse on the chamber. We have taken advantage of the short duration of the pulses involved by using the simple capacitively coupled probe shown in Fig. 11. A small metal plate was mounted near the ground plane of the transmission line between the shorting gap and the chamber. The plate was capacitively coupled to the ground through capacitance C and to the high voltage electrode through a capacitance C'. The voltage division ratio is

$$\frac{V}{V_o} = \left(\frac{C}{C + C'}\right)\left(\frac{Z_o}{Z_o + R}\right)$$

where Z_o is the impedance of the signal cable. We chose $R = 10^4$ Ω and the ratio $C'/C = 50$ for a voltage division ratio of 1000:1.

The chamber itself was a transparent insulating box 5 1/2-in. high and 20-in. along the beam line. There is a 4 x 4-in. entrance window made of 1/2 mil Mylar to reduce spurious scattering of the incident beam and 10-mil Mylar sides to permit the protons, but not the recoil helium nuclei, to pass

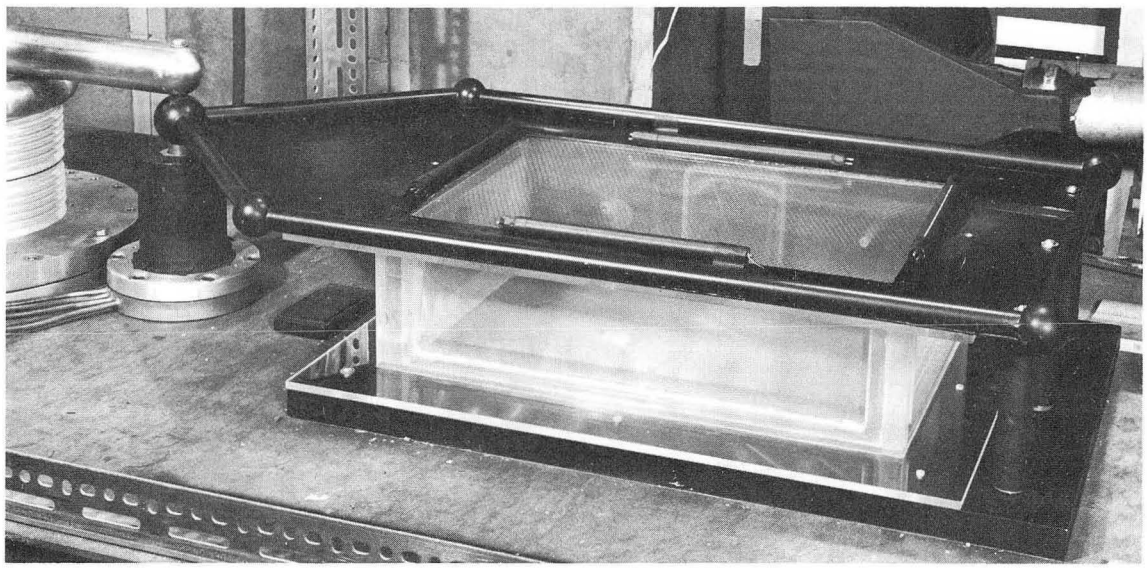

GPR-3141

Fig. 10. Chamber and transmission line assembly.

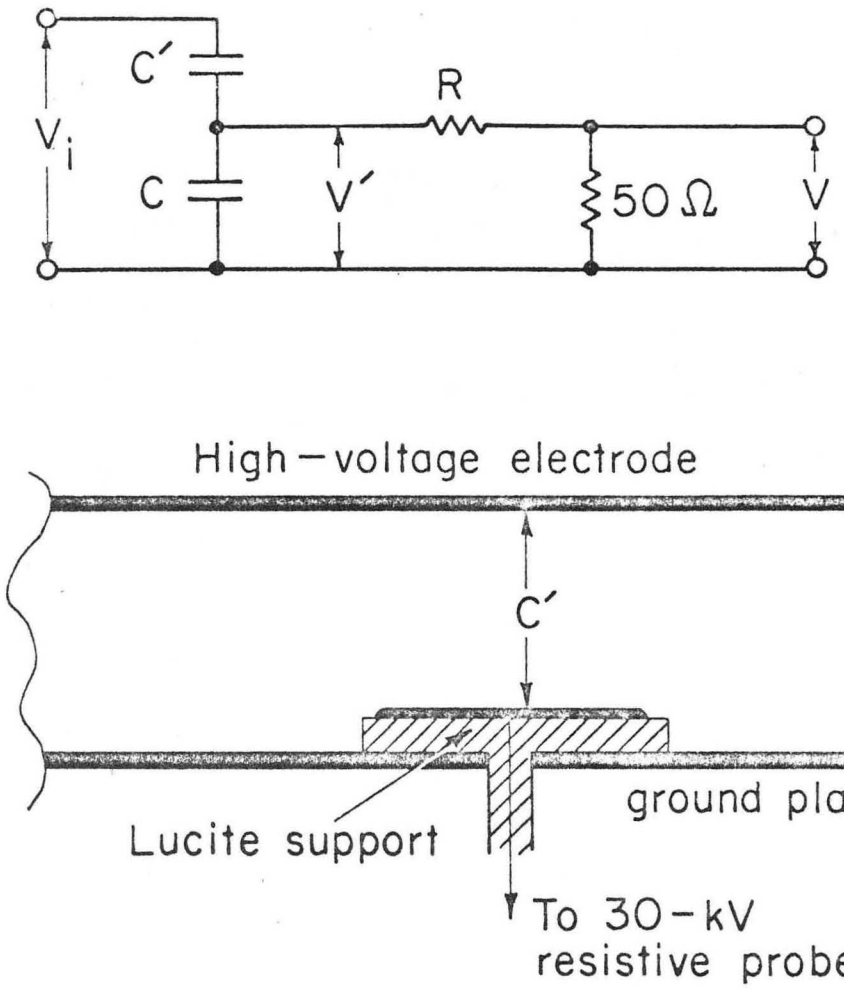

Fig. 11. Capacitive voltage divider.

into the trigger counters.

The chamber was filled with helium with about 0.2% alcohol vapor to reduce memory time. During operation the helium was purified and circulated through the chamber at a rate of 12 cu. ft./hr. to remove impurities which might have a quenching effect on the streamers.

3. Image Intensifier System

The light produced by streamers in helium is too faint to photograph with reasonable demagnification using conventional film.[22] We used the RCA C70021 image intensifier tube to provide the necessary amplification. This is a three-stage electrostatically and magnetically focussed tube with a 2-1/2-in. diameter photocathode and anode. It provides a resolution of 20 line pairs per millimeter and a nominal gain of 20,000:1 in light intensity. The chamber was imaged on the cathode by a f1.4 Nikon lens with a focal length of 50 mm. The image on the anode of the tube was projected onto 35 mm film by a special f1.2 Zeiss lens with 108 mm focal length. With this system we were able to resolve 6 line pairs per cm at the position of the chamber. The net gain in light intensity over a single f1.4, 50 mm lens was about 30:1. The final image was recorded on Kodak 2475 film,which was chosen for its acutance and high sensitivity in the spectral region of the output phosphor of the image tube.

There is some distortion inherent in the image tube, but it is not noticeable near the center of the image field. In principle the distortion could be compensated analytically after the film was measured, but we found it preferable to demagnify the image of the chamber so that the scattering vertices never appeared in those regions of the image field in which the distortion was not negligible. In this way we sacrificed some resolution in order to simplify the analysis of the film.

Two representative events including scattering vertices, fiducials, and event-number and data lights are shown in Fig. 12.

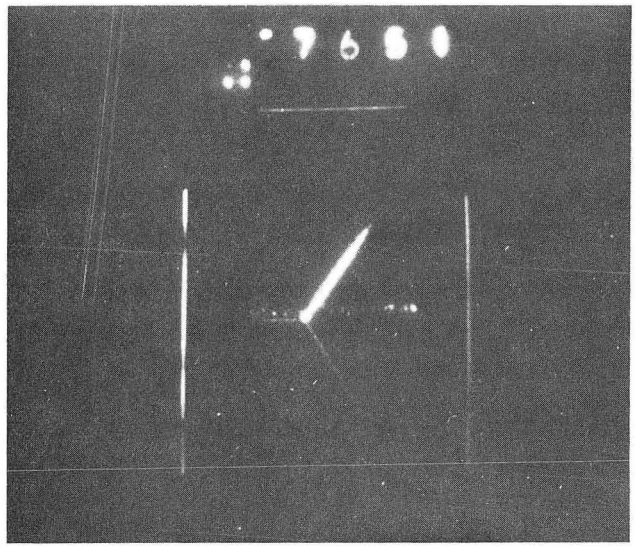

(a) Elastic scattering.

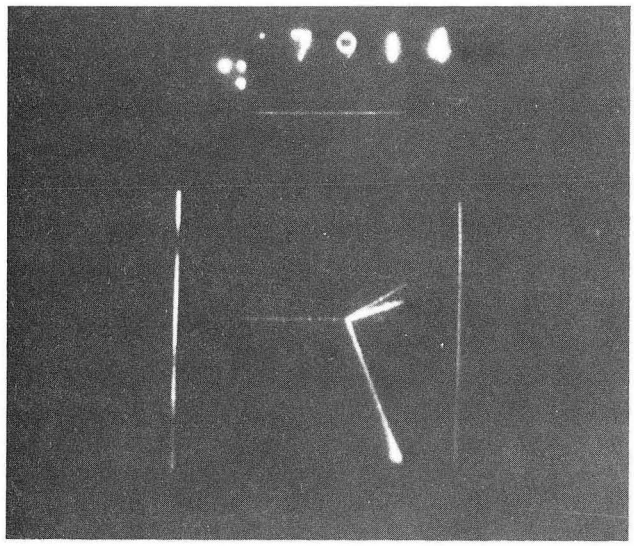

XBB 685-2895

(b) An inelastic event, presumably $p + He^4 \rightarrow 2p + t$.

Fig. 12. Proton-helium scattering events photographed with the image intensifier.

E. Running Conditions

The data taking time for this experiment was divided roughly equally between the two beam energies, 70 and 80 MeV. To determine the contamination of inelastically scattered protons in the secondary beam, about 25% of the 80 MeV running time was taken with a carbon target.

A few runs were taken to determine the relative fluxes of protons from hydrogen, carbon, and sources other than the target. For this purpose the primary beam flux was normalized by integrating the output of a secondary emission counter placed directly behind the target. The results are listed in Table I.

During the runs the two side counters were interchanged periodically so that any differences in their efficiencies would be averaged out of the final asymmetry. These two counter arrangements are called the "normal" and "interchanged" counter positions in Tables II and IV.

The intensity of the tracks in the streamer chamber depended very critically on the exact shape of the high voltage pulse. In order to maintain consistent operation, it was necessary to monitor the pulse frequently so that minor adjustments in the shorting gap pressure and Marx generator supply voltage could be made to compensate for minor changes in spark gap characteristics.

Table I. Relative fluxes of protons from hydrogen, carbon, and sources other than the target.

Target	Protons per Preset Stop	Fraction of Total CH_2 Beam
CH_2 Target	3.16×10^5	-
Carbon Target	1.87×10^5	-
No Target	1.04×10^4	-
Free protons in CH_2	-	.717
Carbon nuclei in CH_2	-	.250
Background	-	.033

III. DATA ANALYSIS

The calculation of the analyzing power of helium was performed in two steps: First, the streamer chamber film was scanned and candidates for p-He scattering events were measured. Second, the kinematics of each event were reconstructed and geometrical corrections of the analyzing power were calculated. The analyzing power was then obtained from this sample by gathering the events into bins according to c.m. angle and correcting for the polarization of the inelastically scattered protons. These steps are described in detail below.

A. Film Scanning

During this experiment 620,000 photographs were taken. Each photograph consisted of one view of the streamer chamber and recorded scattering vertices in addition to many unscattered beam tracks.

These pictures were scanned and events suitable for analysis were measured with the TRAMP digitized protractor. For each frame in which there occurred an acceptable event, the positions of three fiducial strip lights were measured along with the slopes and end points of the three tracks constituting the scattering vertex. These measurements contained a certain amount of redundant information which was used as a consistency check on the data.

In order to avoid contaminating the data with inelastic events or events resulting from the collision of an incident proton with the chamber walls, the following criteria for acceptable events were established:

1. The proton's entrance angle and point of entry into the chamber were required to be within certain limits to eliminate events due to protons which had scattered out of the beam channel.

2. Each vertex had to be distinct with no evidence of a third particle in the final state.

3. The event was rejected if any of the three tracks were too short or too broad to be assigned a direction accurately.

4. Each event was required to trigger only one of the two side counters. This eliminated some inelastic events in which both final state particles can penetrate the chamber walls.

Table II gives the number of events satisfying the above criteria, along with the total pictures taken for each energy and target material.

Table II. The number of pictures taken and events measured for each energy and target material.

Energy (MeV)	Target	Counter Position	Frames Scanned	Frames Measured
80	CH_2	Normal	142,841	1920
80	CH_2	Interchanged	102,283	2045
80	C	Normal	67,801	1166
80	C	Interchanged	46,928	993
70	CH_2	Normal	127,643	3198
70	CH_2	Interchanged	140,068	3631

B. Data Reduction

A computer program was written to carry out the following calculations for each event measured.

1. The position of the point of interaction with respect to the walls of the chamber and the scattering angles were reconstructed from the output of the TRAMP encoders.

2. From this information, together with the geometry of the chamber and side counters, the azimuthal angular acceptance was calculated for each event.

3. On the assumption that the event was due to elastic proton-helium scattering, the azimuthal angle ϕ and the c.m. scattering angle θ were calculated by minimizing the function

$$\chi^2 = \left(\frac{\theta^{P}_{obs} - \theta^{P}_{calc.}}{\Delta\theta^{P}} \right)^2 + \left(\frac{\theta^{He}_{obs} - \theta^{He}_{calc}}{\Delta\theta^{He}} \right)^2$$

subject to the constraint that ϕ fall within the range of acceptable azimuthal angles obtained in Step 2. In this equation θ^{P}_{obs} and θ^{He}_{obs} are the observed (projected) scattering angles, θ^{P}_{calc} and θ^{He}_{calc} are the projected scattering angles calculated from the assumed θ and ϕ, and $\Delta\theta^{P}$ and $\Delta\theta^{He}$ are the estimated errors inherent in measuring the tracks. It is possible in principle to calculate θ and ϕ directly from $\theta_{obs}{}^{P}$ and $\theta_{obs}{}^{He}$ without resorting to a minimization process. In practice the errors $\Delta\theta^{P}$ and $\Delta\theta^{He}$ propagate in such a way that the final uncertainty in ϕ is comparable to the azimuthal angular acceptance calculated from the counter geometry.

The number of χ^2 was also calculated for each event under the assumption that the reaction $p + He^4 \rightarrow d + He^3$ was observed instead of elastic scattering. Kinematically acceptable events had to satisfy the

criteria

$$\chi^2(p + He^4 \rightarrow p + He^4) \leq 0.05$$

$$\chi^2(p + He^4 \rightarrow d + He^3) \geq 0.05.$$

The choice of the cutoff at $\chi^2 = 0.05$ is discussed in Sec. IV. A. 2.

4. Protons which are not incident along the center line of the chamber can produce spurious asymmetries. At forward scattering angles a proton can trigger one side counter even though it would have missed the counters altogether if it had scattered at the same angle but to the opposite side. In general the azimuthal angular acceptances of the right and left side counters will not be the same for a proton scattering at a point off the chamber center line.

In order to avoid biases in the scattering asymmetry due to asymmetrical beam position, the following procedure was employed: For each event the azimuthal acceptance ϕ_o was calculated on the assumption that the proton had scattered to the opposite side. If this was zero the event was rejected. Otherwide the numbers ϵ_{ϕ_o} and $\sin \phi_o$ were calculated for each event. (ϵ = +1 or -1 depending on whether the proton scattered left or right respectively.) The final asymmetry averaged over the azimuthal angle and corrected for the differences in counter acceptance is then

$$a(\theta) = \frac{\sum_i \epsilon_i \phi_{o_i}}{\sum_i \sin \phi_{o_i}}$$

where the sums range over all events in the angular bin labeled by θ. This equation is derived in Appendix B.

5. The net polarization of the CH_2 beam was determined as follows: Denoting

$$\epsilon = \frac{\text{inelastic protons}}{\text{total protons in beam}},$$

the polarization of the CH_2 beam, say $P(CH_2)$, is given by

$$P(CH_2) = \epsilon\, P(C) + (1 - \epsilon)\, P\ (H)$$

where P(C) and P(H) are the polarizations induced by carbon and hydrogen. P(C) is determined by comparing the asymmetries due to carbon with those due to CH_2 in any given bin by means of the formula

$$P(C) = \frac{a_i(C)\ P(H)\ (1 - \epsilon)}{a_i(CH_2) - \epsilon\ a_i(C)},$$

where the a_i's are the asymmetries in the ith bin. The final value for P(C) quoted in Sec. V is a weighted average over all angular bins.

IV. ERRORS AND CORRECTIONS

A. Inelastic Reactions

The inelastic channels which are open to the proton-helium system at 70 and 80 MeV, together with their respective Q values, are listed in Table III.

Table III. Possible inelastic reactions and Q values for protons on He^4.

	Reaction	Q(MeV)
1.	$d + He^3$	- 18.32
2.	$2p + t$	- 19.81
3.	$p + n + He^3$	- 20.55
4.	$p + 2d$	- 23.75
5.	$2p + n + d$	- 25.97
6.	$3p + 2n$	- 28.2

Of these reactions, only (1) and (3) are potentially troublesome sources of background to elastic scattering. The others all have three charged particles in the final state, and can be recognized and rejected when the event is measured.

1. The Reaction $p + He^4 \rightarrow p + n + He^3$

Experimental evidence for reaction (3) is somewhat indirect. In order to estimate this background contamination, we must rely on experiments[23-25] in which the energy spectrum of final state protons was observed at various angles when helium was bombarded with protons of known energy. This data has been explained satisfactorily[26] by assuming that the observed inelastic spectrum is due to quasi-elastic scattering leading to final states (2) and (3). In this case the ratio of reactions (2) and (3) at any specified proton angle should be approximately equal to the ratio of the elastic proton-proton and proton-neutron differential cross sections.

According to Hayakawa et al.[24] who measured the spectrum at 55 MeV incident proton energy, the ratio of inelastic protons to the elastic protons is about 0.02 at 30 deg in the laboratory system and reaches a maximum of the order of 0.1 at 60 deg and then decreases rapidly with increasing angle. Since the proton-proton and proton-neutron differential cross-sections are roughly flat and comparable in magnitude between 50 and 80 MeV, we estimate that reaction (3) can add at most 5% to the elastic protons at any given proton angle.

Not all of these 5% will actually pass as elastic events, however. It is also necessary that the trajectory of the recoil He^3 projected onto the horizontal plane makes an angle with the incident beam direction which is approximately equal to the He^4 scattering angle for an elastic event with the same proton angle. In order to estimate how often this can occur, we have written a Monte Carlo program which generates events of type 3 in such a way as to uniformly populate the $p + n + He^3$ phase space. For each event the proton scattering angle (in the lab system) and the He^3 polar angle projected onto the proton scattering plane were used as input to the same kinematics routine which was used to analyze the actual data. For each proton angle some three-body events simulated kinematically acceptable elastic events. The probability for this to happen as determined by the Monte Carlo program is plotted in Fig. 13 as a function of the apparent (elastic) c.m. angle. Since this efficiency is on the order of 10% at its maximum, the ratio of accepted events of type 3 to elastic events is at most one in 200. Since the statistical accuracy of the polarization data is not comparable to 0.5%, we may neglect this background in calculating our final asymmetry.

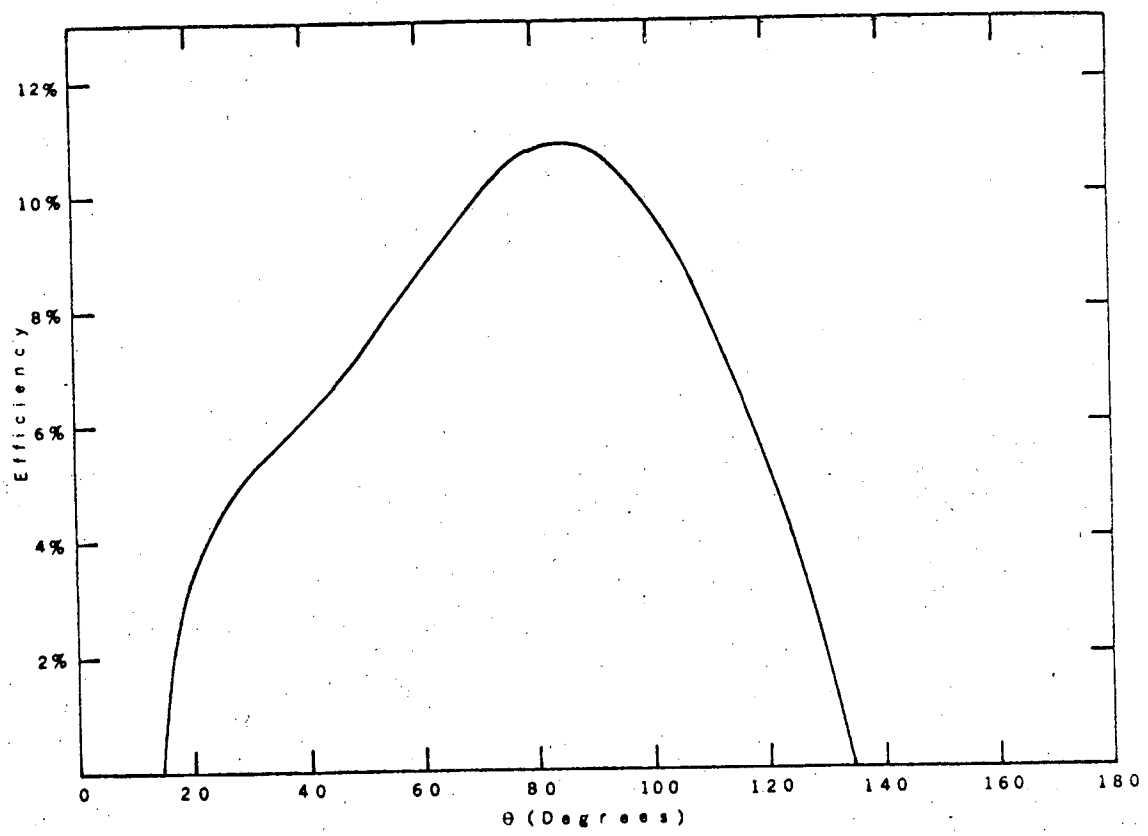

Fig. 13. Efficiency for confusing the reaction $p + He^4 \rightarrow p + n + He^3$ with elastic scattering as calculated by the Monte Carlo program. θ is the c.m. angle calculated on the erroneous assumption that the three-body event was elastic.

2. The Reaction $p + He^4 \rightarrow d + He^3$

Reaction (1), like elastic scattering, produces a co-planar, two-particle vertex. At all observable scattering angles the deuteron possesses enough energy to escape the chamber and trigger the system whereas the He^3 does not. Therefore, reaction (1) can be distinguished from elastic scattering only by comparing scattering angles.

In order to estimate the probability of confusing the two kinds of events, a Monte Carlo program was written similar to the one described in the preceding section. The program generated $d + He^3$ events isotropically in the c.m. angle, and then calculated the "observed" scattering angles taking into account the effect of the azimuthal angle and the probable errors in photographing and measuring the tracks. The apparent proton and He^4 scattering angles were fed into the regular analysis program. The probability obtained in this way for regarding a type 1 event as a kinematically acceptable elastic scatter is plotted in Fig. 14 as a function of the apparent (elastic) c.m. angle. This probability is as much as 80% at 75 deg and drops sharply to zero within 15 deg on either side.

The differential cross section for reaction (1) has been measured at 55 MeV[24] and 95 MeV[25] as well as several lower energies. At 55 MeV the $d + He^3$ cross section is clearly comparable to the elastic cross section in the vicinity of 75 deg; and, although the data at 95 MeV are incomplete, a reasonable extrapolation of the cross section to 75 deg leaves it in the same order of magnitude as the elastic DCS at this energy as well.

On the basis of this information , it was decided to eliminate this background by attempting to fit each provisional elastic event with $d + He^3$ kinematics. Each event which conformed to $d + He^3$ scattering angles to within some critical chi-square was rejected. The Monte Carlo

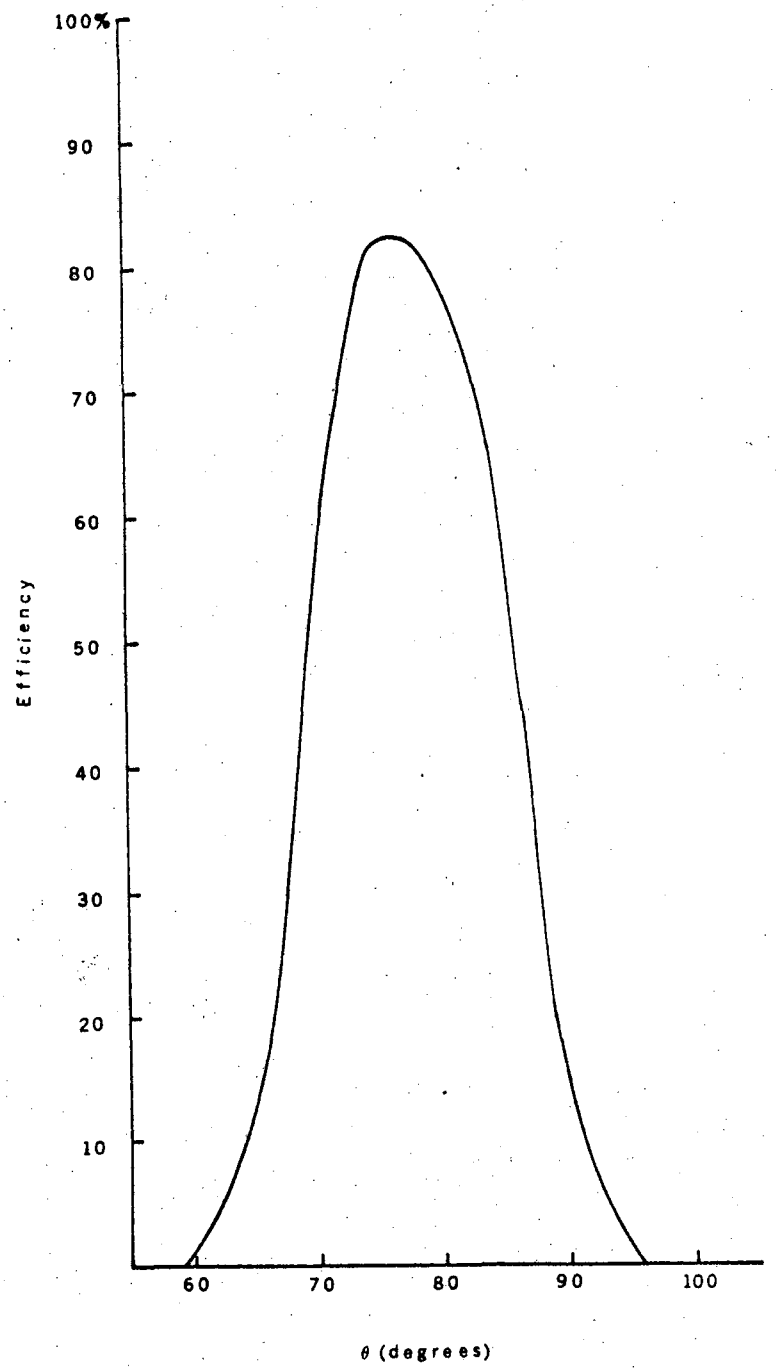

Fig. 14. Efficiency for confusing the reaction $p + He^4 \rightarrow d + He^3$ with elastic scattering.

program was used to determine this chi-square criteria so that as few elastic events as possible were rejected while maintaining a negligibly small probability that an inelastic event would satisfy elastic kinematics and yet fail to qualify as a d + He^3 event. A cutoff of $\chi^2_{max} = 0.05$ was chosen for the final analysis. The number of "pure" elastic events, pure d + He^3 events, and ambiguous events obtained at each energy is listed in Table IV.

B. Miscellaneous Corrections

In addition to the inelastic background, there are several factors which could, in principle, introduce errors into final polarization results. They are listed below:

1. Polarization of the primary cyclotron beam. This has been measured by several experimenters.[34,35] No polarization has been detected.

2. Precession of the polarization of the secondary beam in the field of the quadrupole magnets. The angle of precession $\Delta\theta p$ of the direction of the spin of a proton in a magnetic field[36] is given by

$$\Delta\theta p = \frac{\theta\,\gamma}{2}\,(g - 2)\,,$$

where θ is the bending angle in the plane containing the polarization, $\gamma = (1 - \beta^2)^{-\frac{1}{2}}$, and g = 5.58. In this experiment θ is a few degrees at most, so the net change in beam polarization is negligible.

3. Depolarization of the secondary beam due to passage through matter. This effect has been estimated by Wolfenstein[20] and is negligible.

4. Scattering from impurities in the helium. Reactor Grade helium was used. (Guaranteed less than 5 parts in 10^5 contamination.) The gas was continuously circulated through a molecular sieve and liquid nitrogen trap to remove traces of air and water vapor. 0.2% alcohol vapor was added to reduce the memory time, but this is also a negligible quantity compared with the final statistical errors.

Table IV. Number of Events Satisfying Final Criteria.

Type of Events.	Energy (Mev)	Target	Counter Position	Number of Events
Elastic	70	CH_2	Normal	1172
Elastic	70	CH_2	Interchanged	1400
Elastic	80	CH_2	Normal	608
Elastic	80	CH_2	Interchanged	760
Elastic	80	Carbon	Normal	397
Elastic	80	Carbon	Interchanged	416
d + He^3	70	CH_2	Normal	206
d + He^3	70	CH_2	Interchanged	241
d + He^3	80	CH_2	Normal	165
d + He^3	80	CH_2	Interchanged	203
d + He^3	80	Carbon	Normal	83
d + He^3	80	Carbon	Interchanged	64
Ambiguous	70	CH_2	Normal	140
Ambiguous	70	CH_2	Interchanged	196
Ambiguous	80	CH_2	Normal	37
Ambiguous	80	CH_2	Interchanged	81
Ambiguous	80	Carbon	Normal	36
Ambiguous	80	Carbon	Interchanged	44

C. Angular Resolution

There are two significant sources of error in determining the scattering angles. One is due to the broadening of the tracks caused by long streamers developing from the initial avalanches, the other is simply the error a human operator makes in determining the center of a track of finite width.

1. Streamer Broadening

The proton tracks with their low specific ionization never develop to the completed streamer stage. The alpha tracks, on the other hand, become "curtains" of light extending from the top to the bottom of the chamber. If such a curtain is not viewed directly parallel to the electric field it appears as a broad track. The center of this track will not coincide with the actual trajectory unless the trajectory lies in the midplane of the chamber. The angular error which this introduces can be easily estimated from the chamber geometry. This is done in detail in Appendix C. The RMS deviation for alpha tracks obtained there is .021 radians.

2. Measuring Error

In addition to the effect described above the tracks are also broadened by the finite resolution of the optical system and the image intensifier, and the radial diffusion of the avalanches and streamers. These effects broaden the track symmetrically with respect to the actual trajectory so that the associated error is only due to the uncertainty in finding the center of a wide track. These errors were estimated by having each scanner measure the same sequence of events several times during the analysis phase of the experiment. The number of measurements and the standard error on each track are tabulated below.

Table V. Standard Deviations on Repeated Measurements of a Representative Sample of Events.

Event Number	Number of Measurements	Standard Deviation On Proton Angle (radians)[a.]	Standard Deviation On Alpha Angle (radians)[b.]
1	16	1.15×10^{-2}	$.98 \times 10^{-2}$
2	16	1.10×10^{-2}	2.81×10^{-2}
3	18	1.50×10^{-2}	1.77×10^{-2}
4	17	1.34×10^{-2}	1.19×10^{-2}
5	14	$.82 \times 10^{-2}$	$.90 \times 10^{-2}$
6	15	$.84 \times 10^{-2}$	$.85 \times 10^{-2}$
7	16	$.66 \times 10^{-2}$	$.69 \times 10^{-2}$
8	17	1.05×10^{-2}	$.92 \times 10^{-2}$
9	16	$.55 \times 10^{-2}$	1.99×10^{-2}
10	16	1.25×10^{-2}	2.10×10^{-2}

a. Average σ for the ten events = 1.03×10^{-2} radians.

b. Average σ = 1.43×10^{-2} radians.

The combined uncertainties due to the two effects are σ (proton) = 0.01 rad and σ (alpha) = 0.025 rad. These errors propagate in a complicated way to the determination of θ (c.m.). The details are worked out in Appendix C and the results plotted in Fig. 23. The uncertainty in θ is less than 1.5 deg over a range of 0 to 120 deg; at larger angles the error increases catastrophically.

V. EXPERIMENTAL RESULTS

A. Comparison of Counter Efficiencies

To check for possible differences in the efficiencies of the side counters S1 and S2, the difference

$$\Delta_i = a_i \text{ (normal counter position)} - a_i \text{ (interchanged counter position)}$$

was computed for each bin. (The a_i's are the corrected asymmetries in the ith bin.) The weighted average of Δ_i over the 70 MeV data was 0.02 ± 0.04. This is small enough that the "normal" and "interchanged" data can be combined without further regard to spurious asymmetries due to counter efficiencies.

B. Normalization

The determination of the polarization of the inelastically scattered protons was described in Sec. III. B. Comparing the 80 MeV data from carbon and CH_2 targets yields a value of $P(C) = 11.3\% \pm 9.2\%$. The resulting polarization of the CH_2 beam including the 3% of the beam (presumably unpolarized) scattered from objects other than the target is $-37.3\% \pm 3.3\%$. The error includes the uncertainty in the proton-proton polarization quoted in Ref. 18 together with the error in P(C).

C. Data and Curve Fitting

Tables VI and VII give the polarization $P(\theta)$ determined in this experiment for elastic p-He^4 scattering at 70 and 80 MeV. These quoted values do not include the error on normalization. Only the statistical uncertainty is shown. The derivation of the formula used in computing the statistical accuracy is given in Appendix D.

A phase shift analysis was attempted to get a best fit to all the available data between 60 and 100 MeV. This includes:

1. Polarization at 63.3 MeV[27]
2. Polarization and differential cross section at 66 MeV[28]
3. Polarization data of this experiment
4. Polarization at 96 MeV[29]
5. Differential cross section at 93 and 98 MeV[25]

The curves computed from the phase shifts are shown in Figs. 16 and 17, along with the data points. A more detailed discussion of these phase shift solutions is given in the next section.

Table **VI.** Proton polarization in p + He^4 elastic scattering as a function of c.m. angle for 70 MeV incident kinetic energy.

θ (deg)	Polarization	Error
23 ± 3	.716	.21
28 ± 2	.260	.15
32 ± 2	.008	.13
36 ± 2	.136	.14
40 ± 2	-.198	.14
44 ± 2	-.192	.17
48 ± 2	.049	.19
53 ± 3	.016	.21
59 ± 3	.111	.25
65.5 ± 3.5	.043	.32
95.5 ± 7.5	-.163	.37

Table **VII.** Proton polarization in p + He^4 elastic scattering as a function of c.m. angle for 80 MeV incident energy.

θ(deg)	Polarization	Error
25 ± 3	- .124	.20
30 ± 2	- .084	.19
34 ± 2	.608	.18
38 ± 2	.150	.20
42 ± 2	.093	.21
47 ± 3	.011	.19
53 ± 3	- .035	.27
60 ± 4	- .119	.26
69 ± 5	- .531	.35

VI. DISCUSSION

Evidently, a few data points at some isolated energy provide very little insight into the structure of an interaction. A useful technique for organizing and understanding the results of separate experiments on a particular scattering system is to parameterize the data in terms of a given number of partial-wave amplitudes. The phase shifts obtained in this way should vary smoothly with energy. Their behavior can be qualitatively understood in terms of intermediate-state resonances, absorption in various angular momentum states, etc.

A. Phase Shift Formalism

The equations used to obtain the polarization and differential cross sections as functions of the phase shifts[31] are as follows: The differential cross section

$$\sigma(\theta) = |g(\theta)|^2 + |h(\theta)|^2$$

and the polarization

$$P(\theta) = \frac{2\mathrm{Re}\left[g^*(\theta)\, h(\theta)\right]}{|g(\theta)|^2 + |h(\theta)|^2}$$

where g and h are the non spin-flip and spin-flip scattering amplitudes respectively, given by

$$g(\theta) = f_c(\theta) + \sum_{\ell=0}^{\ell_{max}} e^{2i\phi_\ell} \left[(\ell+1)A_{\ell+} + \ell A_{\ell-}\right] P_\ell(\cos\theta)$$

and

$$H(\theta) = \sum_{\ell=0}^{\ell_{max}} e^{2i\phi_\ell} \left[A_{\ell+} - A_{\ell-}\right] P_\ell^1(\cos\theta) .$$

The partial wave amplitudes $A_{\ell+}$ are written in terms of the phase shifts as

$$A_{\ell\pm} = \frac{\eta_{\ell\pm}\, e^{2i\delta_{\ell\pm}} - 1}{2ik} .$$

The $\eta_{\ell\pm}$'s are the absorption parameters. They are equal to one if the scattering is purely elastic. In general $0 \leq \eta \leq 1$. The Coulomb amplitudes and phase shifts $f_c(\theta)$ and ϕ_ℓ are given by

$$f_c(\theta) = -\frac{n}{2K} (\text{cosec } \theta/2)^2$$

$$\times \exp\left[-2in \log (\sin \theta/2)\right]$$

$$\exp(2i\phi_\ell) = \frac{\Gamma(\ell + 1 + in)}{\Gamma(\ell - 1 + in)}$$

$$n = \frac{mz_1z_2e^2}{k^2}$$

The resulting equations for $\sigma(\theta)$ and $P(\theta)$ as functions of $\eta_{\ell\pm}$ and $\delta_{\ell\pm}$ are much too complicated to solve analytically. Instead a computer program was used to make a least-squares fit to the existing data. A subroutine was written that, for each tentative set of phase shifts and absorption parameters, calculates the quantity

$$\chi^2 = \Sigma\left\{\left|\frac{\sigma^c(\theta) - \sigma^{exp}(\theta)}{\Delta\sigma(\theta)}\right|^2 + \left|\frac{p^c(\theta) - p^{exp}(\theta)}{\Delta p(\theta)}\right|^2\right\}$$

as well as $\frac{\partial\chi^2}{\partial\delta_{\ell\pm}}$ and $\frac{\partial\chi^2}{\partial\eta_{\ell\pm}}$ for all values of ℓ between 0 and ℓ_{max}.

The superscripts c and exp indicate the calculated and experimental values of the data point, respectively, and Δ indicates the corresponding uncertainty in the data. The summation is over all experimental quantities being considered. Starting then from some trial set of δ's and η's, a variable metric minimization routine[30] varies the parameters in the direction of the negative of the gradient of χ^2 until a minimum is found. The program is arranged so that the η's are constrained to lie between zero and one and the search does not go too far afield from the initial values of the parameters.

B. Results

The p + He^4 scattering data up to 55 MeV have been extensively analyzed.[11,12,15,31] Except for the results of Giamati, Madsen, and Thaler at 40 MeV, the published phase shift solutions are all qualitatively consistent with one another. Their general features are as follows: The s-wave interaction is strongly repulsive. The $p_{3/2}$ phase shift is resonant about 2.6 MeV lab energy, while the $p_{1/2}$ peaks at a slightly higher energy. (Actually, there is a $p_{1/2}$ resonance at 10.8 MeV lab energy. The phase shift does not go through 90 deg because of its repulsive "hard sphere" component. See Refs. 6, 7, or 8.) The interaction is generally attractive in the p, d, f, g states and stronger in the $j = \ell + 1/2$ states. The $g_{7/2}$ phase shift is consistent with zero up to 60 MeV. The inelasticity parameters can deviate from unity only above 23 MeV. There is relatively little s-wave absorption, and although the points are scattered considerably, the absorption in the higher partial waves increases with increasing energy.

Probably none of the solutions above 20 MeV are unique, but so far it has been possible to recognize spurious solutions by comparing them with results at lower energies. We have done phase shift searches at 63.3, 70, 80, and 93 MeV with this point of view. First at 63.3 MeV a solution was sought in the vicinity of the 55 MeV results given in Ref. 15. When a solution was found it was used as the starting point for the search at 70 MeV and so on. Each solution was perturbed in random steps and re-searched at least ten times. Various bizarre solutions were encountered in this way, but only one set of solutions was found which connected the four energies reasonably. These results are given in Tables VIII through XI.

In order to obtain solutions at 70 and 80 MeV it was necessary to

interpolate between the differential cross section data at 66 and 94 MeV. This can be done **plausibly** since the differential cross sections at 55, 66, 93, and 147 MeV, when plotted as functions of momentum transfer $q = 2k \sin \theta/2$, are nearly congruent over a range of q from 0.4 to 3.0 f^{-1}; i.e., from 10 to 100 deg in the center of mass. No attempt was made to fix the DCS outside of this interval.

The standard errors for each of the phase shifts and absorption parameters are listed in Tables **VIII** through **XI** together with the goodness of fit parameter χ^2. The errors reflect not only the quality of data used for each fit but also the extent to which the data can constrain the phase shifts. The anomalously large errors on some of the 70 and 80 MeV parameters, especially δ_{1-}, are due to the lack of any polarization or DCS data at backward angles rather than any defect in the fit of the extant data. The χ^2 at 94 MeV is too high, mostly because of a poor fit with the small angle DCS data.

A maximum angular momentum of $\ell = 5$ was used at each energy. Including i-wave phase shifts did not noticeably improve the fit, **even at 93 MeV.**

The phase shifts obtained at the four energies are completely consistent among themselves as well as consistent with the results at lower energies. The s-wave phase shift is constant at -135 deg while the $p_{3/2}$ and $p_{1/2}$ terms continue their gradual decline from resonance. The d wave phase shifts persist in the order of 10 to 20 deg with the characteristic inverted doublet structure; the higher partial waves are all small.

The absorption parameters do not present so consistent a picture. Their values are widely scattered between 0.5 and 1.0. Only the s-wave absorption and the absorption in the higher angular momentum states is

relatively constant. The others tend to decrease with increasing energy.

The polarization curves calculated from the phase shifts are shown together with the experimental points at the four energies in Figs. 15 through 18.

Table **VIII.** Phase shifts at 63.3 MeV [a].

State	δ (rad)	error	η	error
$S_{1/2}$	.777	.039	.978	.112
$P_{3/2}$	.813	.073	.962	.115
$P_{1/2}$	.420	.054	.863	.075
$D_{5/2}$	.449	.048	.716	.136
$D_{3/2}$	.185	.043	.749	.037
$F_{7/2}$	.215	.027	.948	.058
$F_{5/2}$	.079	.032	.823	.034
$G_{9/2}$	.041	.026	.904	.037
$G_{7/2}$	-.002	.018	.890	.025
$H_{11/2}$	.038	.019	.827	.040
$H_{9/2}$	.003	.012	.945	.030

a. $\chi^2 = 11.$ with 44 data points.

Table **IX.** Phase shifts at 70 MeV.[a]

State	δ (rad)	Error	η	Error
$S_{1/2}$	.732	.141	1.0	0.10
$P_{3/2}$	.702	.104	.860	.273
$P_{1/2}$	.387	.672	.771	.597
$D_{5/2}$	.316	.124	.699	.125
$D_{3/2}$	.072	.127	.707	.112
$F_{7/2}$	.241	.117	.767	.187
$F_{5/2}$	-.102	.118	.916	.213
$G_{9/2}$	.080	.073	.689	.160
$G_{7/2}$	-.130	.117	.919	.115
$H_{11/2}$	.114	.062	.675	.146
$H_{9/2}$	-.142	.088	.992	.086

a. $\chi^2 = 7.6$ with 40 data points.

Table X. Phase shifts at 80 MeV.[a]

State	δ (rad)	Error	η	Error
$S_{1/2}$	.708	.563	.938	.296
$P_{3/2}$	.397	.072	.661	.375
$P_{1/2}$	.689	.729	.985	.031
$D_{5/2}$	.177	.260	.703	.125
$D_{3/2}$	.487	.051	.990	.202
$F_{7/2}$	.105	.502	.790	.116
$F_{5/2}$	.320	.189	.715	.264
$G_{9/2}$	.065	.281	.881	.133
$G_{7/2}$	-.027	.217	.598	.601
$H_{11/2}$	-.051	.170	.995	.022
$H_{9/2}$	-.034	.436	.710	.413

a. χ^2 = 12.2 with 39 data points.

Table **XI.** Phase shifts at 93 MeV.[a.]

State	δ (rad)	Error	η	Error
$S_{1/2}$	.740	.073	1.0	0.10
$P_{3/2}$	.555	.066	.781	.091
$P_{1/2}$	.523	.102	.922	.124
$D_{5/2}$	.297	.080	.654	.056
$D_{3/2}$	.285	.126	.565	.086
$F_{7/2}$	.138	.056	.736	.058
$F_{5/2}$	-.002	.092	.522	.091
$G_{9/2}$	.094	.029	.834	.053
$G_{7/2}$	-.069	.047	.674	.099
$H_{11/2}$	.020	.015	.951	.038
$H_{9/2}$	.012	.028	.941	.058

a. $\chi^2 = 46.6$ with 38 data points.

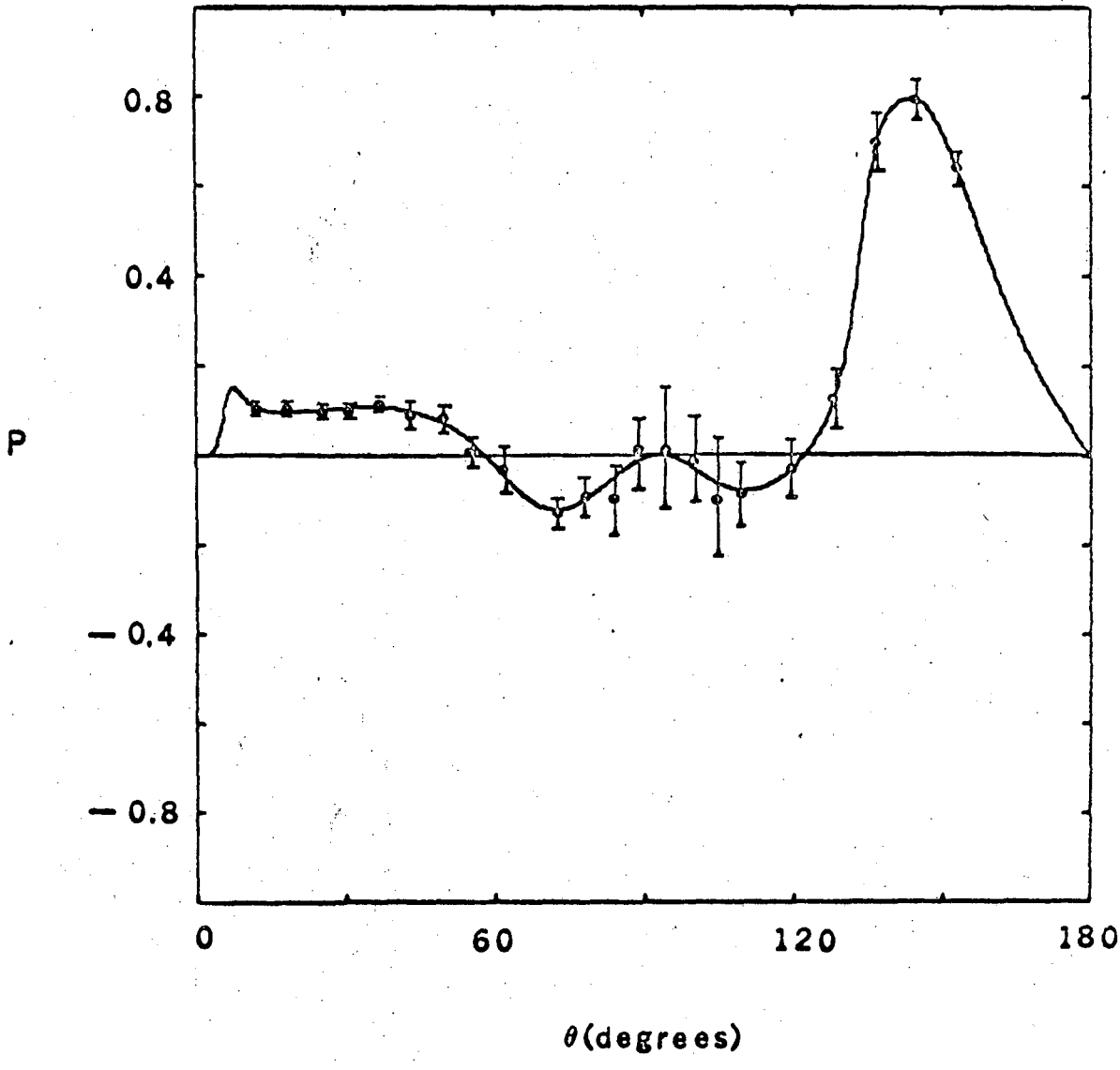

XBL 688-5643

Fig. 15. Recoil proton polarization in p + He^4 elastic scattering at 63.3 MeV as a function of c.m. angle. The data points are from Ref. 27. The solid line is a polarization curve computed from the phase shifts in table VIII.

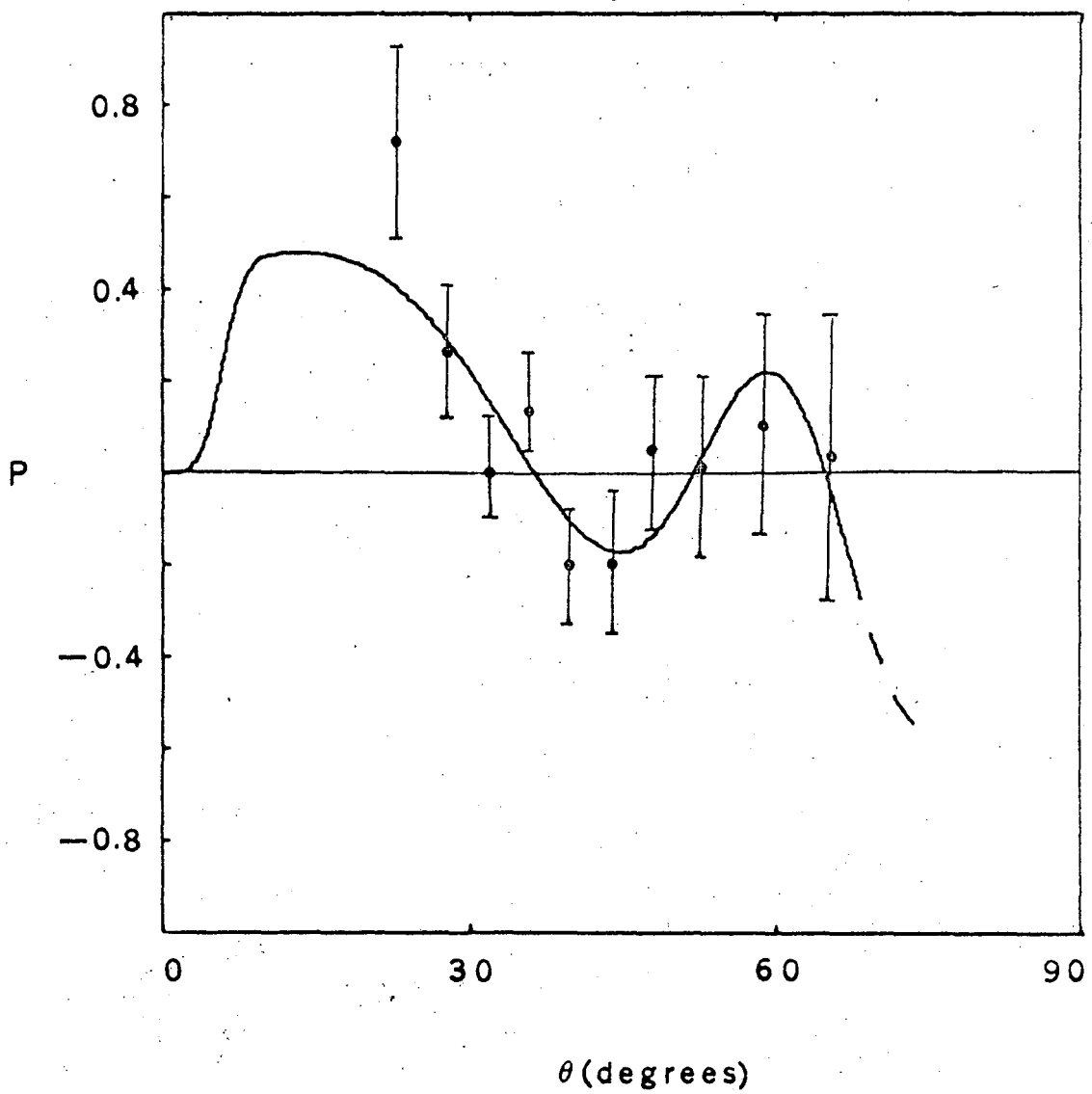

XBL 688-5641

Fig. 16. Recoil proton polarization in p + He^4 elastic scattering at 70 MeV as a function of c.m. angle. The data points are from this experiment. The solid line is a polarization curve computed from the phase shifts in table IX.

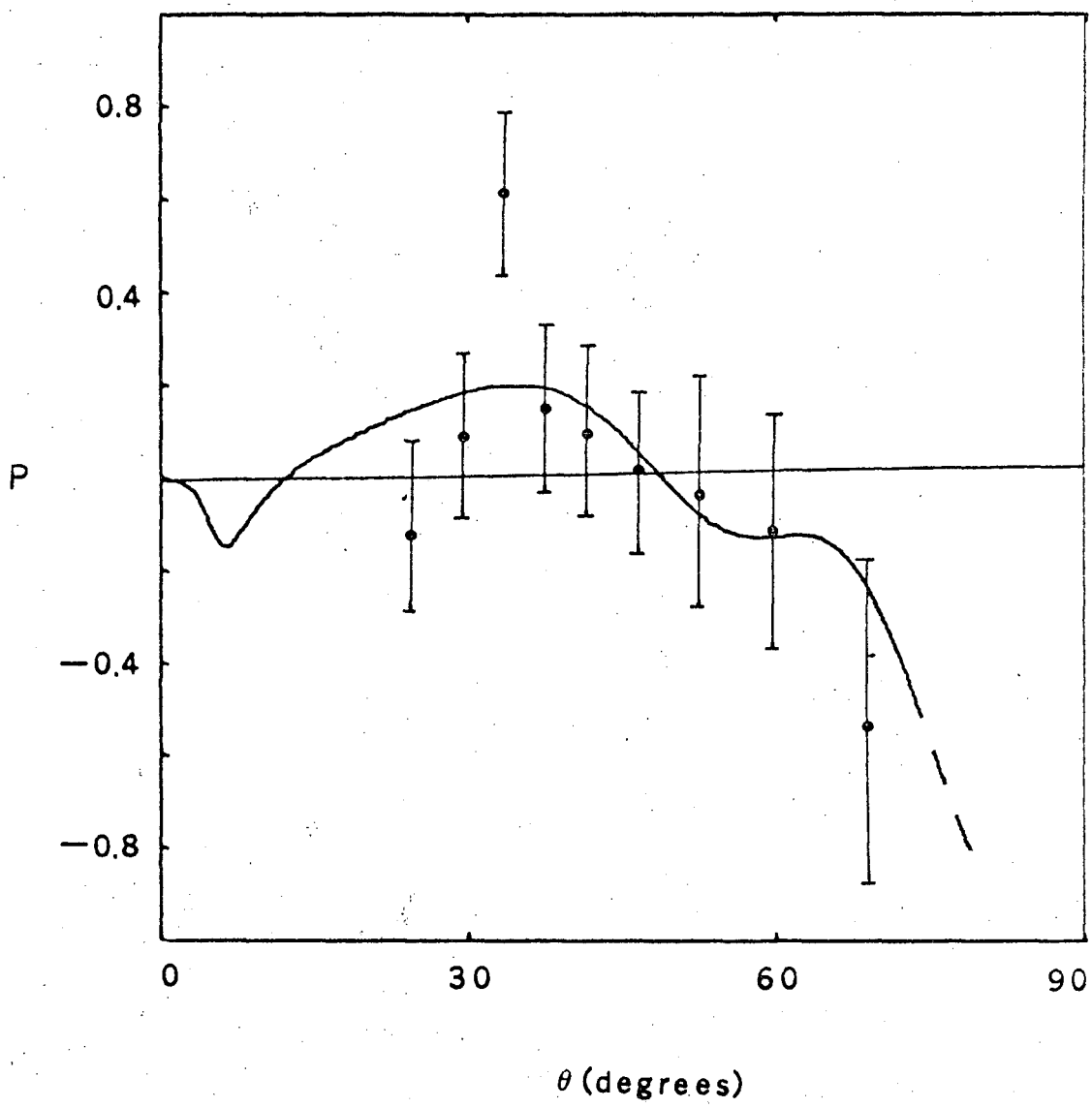

XBL 688-5640

Fig. 17. Recoil proton polarization in p + He^4 elastic scattering at 80 MeV as a function of c.m. angle. The data points are from this experiment. The solid line is a polarization curve computed from the phase shifts in table X.

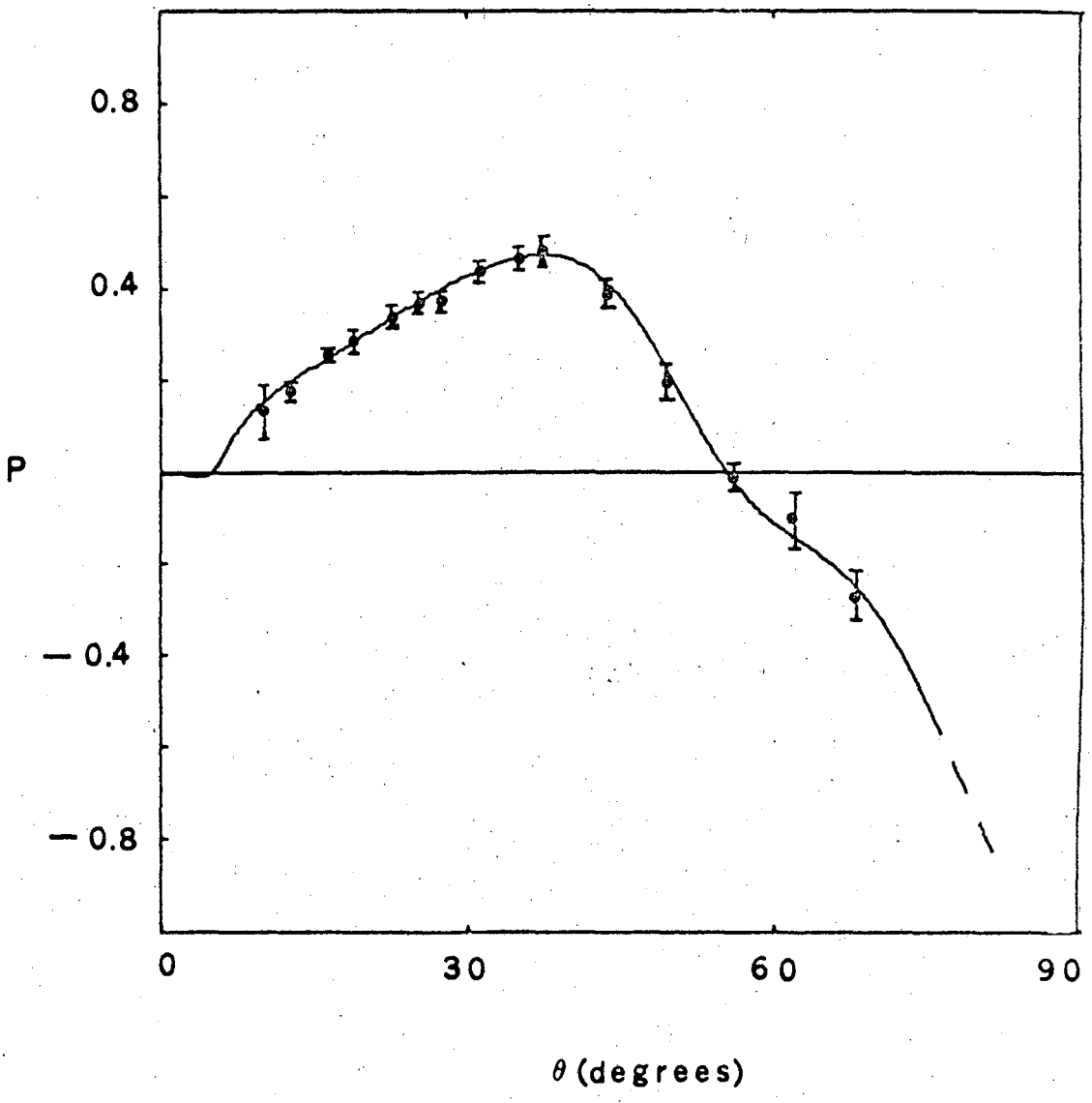

XBL 688-5642

Fig. 18. Recoil proton polarization in p + ^{4}He elastic scattering at 96 MeV as a function of c.m. angle. The data points are from Ref. 29. The solid line is a polarization curve computed from the phase shifts in table XI.

SUMMARY AND CONCLUSIONS

We have used a helium-filled streamer chamber -- a device that has not been previously used in a practical experimental situation -- to observe the scattering of protons in gaseous helium. With the help of an image intensifier and special high-voltage equipment, we were able to obtain consistently good photographs over many hours of operation. The system made possible good resolution, in the projection mode, of tracks which differed greatly in ionization density. Since the gas in the streamer chamber was used as the scattering target, we were able to observe vertices involving some very low-energy particles. This technique will be useful in many experiments with low-, and intermediate-energy interactions.

The recoil proton polarization in $p + He^4$ elastic scattering was measured at 70 and 80 MeV incident proton energy. With this data, as well as that at 96 MeV and lower energies, the polarization at forward angles is essentially determined from zero to 96 MeV. The forward polarization peak, which increases with increasing energy above 70 MeV, makes helium an attractive analyzer for polarized nucleons at these energies. We have completed phase shift analyses of the 63.3, 70, 80 and 96 MeV data and obtained solutions which vary smoothly with energy and are consistent with results at lower energies.

ACKNOWLEDGMENTS

As an accomplishment, a thesis is the realization of the work of many people. I would like therefore to express my gratitude to those noted below.

First, I am grateful to my research advisor, Dr. Victor Perez-Mendez, for the instruction and inspiration I enjoyed as a graduate student under his guidance.

I have enjoyed and benefited by the cooperation of my close associates, Mr. John Sperinde and Dr. Leon Kaufman.

I am greatly indebted to Anne Carter and members of the scanning group for theis constant help during the analysis phase of this experiment.

I acknowledge the graciousness of our secretaries, Mary Louise Quinn and Miriam Machlis, in cheerfully typing and editing this and other manuscripts.

Finally, I would like to express my gratitude to my wife, Elin. In addition to her proofreading and preparing the illustrations for this thesis, her unfailing help and patience during this experiment are deeply appreciated.

REFERENCES

1. Freier, Lampi, Sleater, and Williams, Phys. Rev. 75, 1345 (1949).
2. Critchfield and Dodder, Phys. Rev. 76, 602 (1949).
3. M. Heusinkveld and G. Freier, Phys. Rev. 85, 80 (1952).
4. Sack, Biedenharn, and Breit, Phys. Rev. 93, 321 (1954).
5. J. L. Gammel and R. M. Thaler, Phys. Rev. 109, 2041 (1958).
6. R. D. Adair, Phys. Rev. 86, 155 (1952).
7. D. C. Dodder and J. L. Gammel, Phys. Rev. 88, 520 (1952).
8. P. D. Miller and G. C. Phillips, Phys. Rev. 112, 2043 (1958).
9. A. Herzenberg and E. J. Squires, N. P. 19, 280 (1960).
10. M. K. Craddock, R. C. Hanna, L. P. Robertson, B. W. Davies, Physics Letters 5, 335 (1963).
11. S. Suwa and A. Yokosawa, Phys. Letters 5, 351 (1963).
12. C. C. Giamati, V. A. Madsen, and R. M. Thaler, Phys. Rev. Letters 11, 4 (1963).
13. B. W. Davies, M. K. Craddock, R. C. Hanna, L. P. Robertson, and R. E. Shamu, National Institute for Research in Nuclear Science (U.K.) P. L. A. Progress Report NIRL/R/81, (1964), p. 69.
14. E. T. Boschitz, M. Chabre, H. E. Conzett, E. Shield, and R. V. Slobodrian, Phys. Letters 15, 325 (1965).
15. H. E. Conzett, Analysis of Proton-Alpha Cross Section and Polarization Data from 20 to 60 MeV, UCRL-16767, March 1966.
16. S. Fukui and S. Miyamoto, Nuovo Cimento 11, 113 (1958); S. Fukui and S. Miyamoto, Journal of Physical Society of Japan 16, 2574 (1961).
17. L. Wolfenstein and J. Ashkin, Phys. Rev. 85, 947 (1952).

18. David Cheng, Nucleon-Nucleon Polarization at 700, 600, 500, and 400 MeV (Ph. D. Thesis), UCRL-11926, July 1965.

19. T. J. Devlin, OPTIK: An IBM 709 Computer Program for the Optics of High-Energy Particle Beams, UCRL-9727, September 1961.

20. L. Wolfenstein, Phys. Rev. 75, 1664 (1949).

21. D. L. Wieber and H. W. Lefevre, An Amplitude Independent Nanosecond Timing Discriminator for Fast Photomultipliers, UCRL-16227, October 1965.

22. V. Perez-Mendez and A. Stetz, Development of a Helium-Filled Streamer Chamber System, UCRL-16891, May 1968.

23. S. M. Bunch, H. H. Forster, and C. C. Kim, Nucl. Phys. 53, 241 (1964).

24. S. Hayakawa, N. Horikawa, R. Kajikawa, K. Kikuchi, H. Kobayakawa, K. Matsuda, S. Nagata, and Y. Sumi, Phys. Letters 8, 330 (1964); also J. Phys. Soc. Japan 19, 2004 (1964).

25. W. Selove and V. M. Teem, Phys. Rev. 112, 1658 (1958).

26. P. Hillman, A. Johansson, G. Tibell, H. Tgren, Nuc. Phys. 12, 596 (1959).

27. H. E. Conzett (Lawrence Radiation Laboratory), private communication, July 1968. Also, E. T. Boschitz, J. Chabre, H. E. Conzett, E. Shield, and R. J. Slobodrian, Polarization in p - He^4 Scattering Between 27 and 63 MeV, UCRL-16216, August 1965.

28. A. M. Cormack, V. N. Palmieri, N. F. Ramsey, R. Wilson, Phys. Rev. 115, 599 (1959).

29. K. Gotow, Scattering of Polarized Protons by Helium at 203 MeV and 96 MeV, University of Rochester NYO-2532, January 1959.

30. W. C. Davidon, Variable Metric Method for Minimization, ANL-5990 Rev., November 1959.

31. N. Horikawa and H. Kanada, J. Phys. Soc. Japan 20, 1758 (1965).

32. F. Bulos, A. Odian, F. Villa, D. Yount, Streamer Chamber Development, SLAC-74, June 1967.

33. Sanborn C. Brown, Basic Data of Plasma Physics, First Edition (Massachusetts Institute of Technology Press, Cambridge, 1966).

34. O. Chamberlain, E. Segre, R. Tripp, C. Wiegand, and T. Ypsilantis, Experiments with 315-MeV Polarized Protons, I. Elastic Scattering by Complex Nuclei, UCRL-2975, February 1956.

35. P. G. McManigal, Polarization and Differential Cross Sections in Proton-Proton and Proton-Nucleus Scattering at 730 MeV, UCRL-10637, March 1963.

36. R. Hagedorn, Relativistic Kinematics, (W. A. Benjamin, Inc., New York, 1964).

37. L. B. Loeb, Basic Processes of Gaseous Electronics, (University of California Press, Berkeley, 1961).

APPENDICES

A. Theory of Streamer Formation

Consider a free electron moving through a gas under the influence of an electric field E. The electron will be accelerated toward the anode; it soon loses its energy by undergoing an ionizing collision and is then reaccelerated. The numbers of electrons in the avalanche grows exponentially according to the law

$$N = e^{\alpha x}, \tag{1}$$

where α is the number of ions produced per centimeter of path length x along the avalanche. α (usually called the first ionization coefficient or Townsend coefficient) is a function of the pressure of the gas and the external field as shown in Fig. 19. The avalanche length increases at a rate equal to the average velocity of a free electron in the field E. In helium the average electron velocity and the electric field are nearly proportional with mobility constant

$$\mu = 7.6\ (10)^5 \quad \frac{\text{cm/sec}}{\text{volts/cm} \cdot \text{mm Hg}} .$$

As the electrons are swept forward in the electric field they also diffuse laterally leaving behind them a cloud of slowly moving positive ions. Assuming that the ions are nearly stationary, their density is given by the solution of the diffusion equation for a point source in free space.

$$\rho(r) \propto \exp\ (-r^2 t/4D). \tag{2}$$

The diffusion constant D also depends on the electric field. For a Maxwellian gas it is proportional to the average energy of the electrons and to the electron mobility.

$$D = 2/3\ \mu\ U_{av}. \tag{3}$$

U_{av} also depends on the electric field as shown in Fig. 20.

Under the influence of moderate electric fields the avalanche

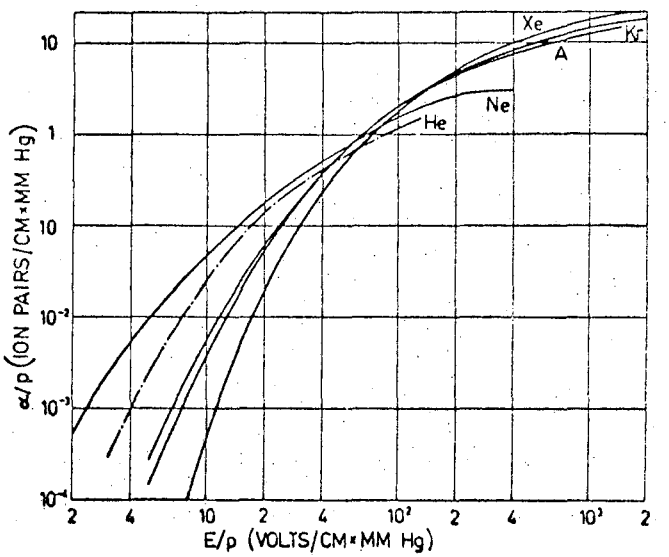

MUB-10900

Fig. 19. The first Townsend coefficient as a function of electric field for various gases. From ref. 33.

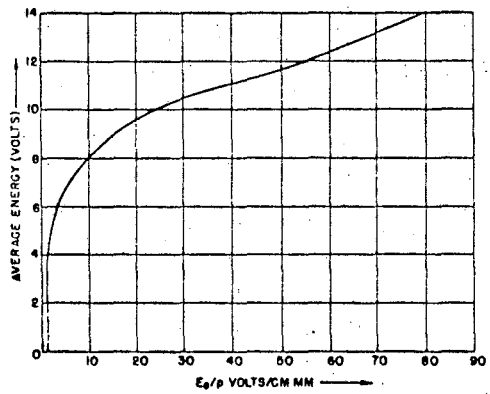

XBL 684-429

Fig. 20. Average electron energy in helium. From ref. 33.

propagates to the anode. For larger E, however, the density of the positive ion cloud increases until its attraction on the faster moving electron could becomes important. When some critical ion density has been attained this "space charge" exactly compensates the external field, and the development of the avalanche stops. This would be the end of the story without some new mechanism to propagate the avalanche. Although the field is zero in the vicinity of the head, it is augmented in the region directly behind the electrons. As soon as a free electron is produced in this region by photo-ionization a new avalanche sprouts up. The electron multiplication proceeds much more rapidly in the high field, and the total region of ionization grows in a rapid, haphazard manner until it extends from the anode to the cathode. This development is called the streamer phase.

There is almost no quantitative information available on photo-ionization processes in helium.[37] Presumably the metastable states of He at 19.5 eV are ionized by the photons from recombining He^+ ions. These photons have a maximum energy of 24.5 eV which is far enough above threshold for the mechanism to be significant. We can expect photo-ionization cross sections two or three orders of magnitude below the electron ionization cross section. This corresponds to a mean free path for photons on the order of several centimeters. Observations of discharges in He streamer chambers show that the propagation of avalanches due to photo-ionization becomes noticeable in a time $t \lesssim 10$ nsec. If the high voltage field persists longer than this the streamers fan out along the field lines behind the initial avalanche, and the discharge grows to fill the space between electrodes.

Ideally, for maximum spatial resolution, the electric field applied to a streamer chamber should persist until the space charge has stalled

further electron multiplication, and then fall to zero before secondary avalanches become noticeable. Observations of the luminosity of tracks in neon-filled streamer chambers described in Ref. 32 suggest that this mode of operation is never actually obtained, at least for photographable tracks. Presumably the pure avalanche mode could be obtained with shorter pulses than those used in Ref. 32, but with a consequent loss in light intensity.

The relationship between the amplitude and duration of the electric field necessary to complete the development of the initial avalanches may be obtained with the help of the following approximations. Denote the radius of the head of the avalanche by r. If we assume that most of the ions are contained in a roughly circular region of radius $r = \sqrt{4Dt}$ at the head of the avalanche, their field

$$E_r = \frac{3Ne}{32\,\pi\,\epsilon_o\,\mu\,U_{av}\,t} \quad . \tag{4}$$

N is the number of ions in the avalanche, and Eq. (3) has been used to eliminate the diffusion constant. Both α and U_{av} depend on the total field at the head of the avalanche, and as E_r begins to cancel the external field α decreases and the rate of streamer growth slows down. We can calculate approximately the various parameters at this stage of streamer development with a simple approximation: assume that α, U_{av}, and the average electron velocity are constant for a time t given by

$$t = x/\mu E \tag{5}$$

until E_r just equals the external field whereupon the avalanche development stops. E is just the external electric field. From Eqs. (4) and (5) the Meek condition will be satisfied when

$$N = \frac{32\pi\,\epsilon_o\,U_{av}\,x}{3e} \quad . \tag{6}$$

U_{av} varies slowly with the external field. U_{av} ~10 volts for most applications.

Now suppose we wish to operate a chamber with a spatial resolution equal to x along the direction of E. The total number of ions in each avalanche is given by Eq. (6). The first Townsend coefficient is then obtained by inverting Eq. (1), and the external field required to sustain this value of α is obtained from Fig. 19. Finally, the duration of the external field equals the time t given by Eq. (5). Some useful values of x, N, E, and t are listed as functions as gas pressure in Table XII.

Table XII. Selected Parameters at Various Gas Pressures.

x (mm)	Pressure (atm.)	N	E (kV/cm)	t (nsec)
1	1	$1.8(10)^7$	19	5
1	2	$1.8(10)^7$	27	7
1	0.5	$1.8(10)^7$	15	3
0.5	1	$9.2(10)^6$	29	2
0.5	2	$9.2(10)^6$	38	3
0.5	0.5	$9.2(10)^6$	25	1
2	1	$3.7(10)^7$	13	15
2	2	$3.7(10)^7$	20	20
2	0.5	$3.7(10)^7$	10	10

B. Polarization Weighting Factors

The probability that a proton will scatter with an azimuthal angle ϕ at some specified polar angle θ is

$$R(\phi) = \frac{1}{N}\left[1 + P_0 P(\theta)\cos\phi\right] . \tag{1}$$

P_0 is the incident beam polarization and $P(\theta)$ is the analyzing power of the target particle. The normalization constant N is determined so that the total probability of the recoil proton striking one or the other side counter is unity; i.e., for an incident proton in the median plane of the chamber

$$\begin{aligned} N &= \int d\phi R(\phi) \\ &= 2\phi_{0_L} + 2\phi_{0_R} + 2P_0P(\theta)\left(\sin\phi_{0_L} - \sin\phi_{0_R}\right), \end{aligned} \tag{2}$$

where ϕ_{0_R} and ϕ_{0_L} equal one-half the total azimuthal angle subtended by the right and left side counters respectively.

The observed asymmetry a_θ is

$$\begin{aligned} a_\theta &= \frac{1}{N}\int_{\text{left counter}} d\phi R(\theta) - \frac{1}{N}\int_{\text{right counter}} d\phi R(\phi) \\ &= \frac{2}{N}\left[\phi_{0_L} - \phi_{0_R} + P_0P(\theta)\left(\sin\phi_{0_L} + \sin\phi_{0_R}\right)\right] . \end{aligned} \tag{3}$$

In terms of N_R, the number of particles scattered right, and N_L the number scattered left, the asymmetry is

$$a_\theta = \frac{N_L - N_R}{N_L + N_R}, \tag{4}$$

substituting (4) and (2) into Eq. (3) and solving for $P_0P(\theta)$ yields

$$P_0P(\theta) = \frac{N_R\phi_{0_L} - N_L\phi_{0_R}}{N_R\sin\phi_{0_L} + N_L\sin\phi_{0_R}} . \tag{5}$$

For most events with ϕ_0 on the order of 20 deg, Eq. (5) represents a correction of 4% to the analyzing power one would calculate ignoring

the finite width of the counters.

If the incident proton does not lie in the median plane of the chamber as was assumed in the derivation, a further small correction is added to Eq. (5). This term is small compared with other experimental uncertainties and can be ignored.

C. Angular Resolution

1. Streamer Broadening

Referring to Fig. **21**, imagine a streamer of length ℓ at a distance r from the optical axis 0 - 0'. If the point of observation 0 is a distance s from the chamber, the projected width of the streamer $\delta = \ell r/s$, so long as $s \gg \ell$.

Now suppose a track of length R begins at a distance x., and ends at a distance $x + R \cos\theta$ from the optical axis. The angle θ is defined in Fig. **22**. The width δ_1 at the beginning of the track is

$$\delta_1 = \frac{\ell x}{S} \sin\theta ,$$

and the width δ_2 at the end

$$\delta_2 = \frac{\ell}{S}(x + R \cos\theta) \sin\theta.$$

The actual trajectory must pass through the ends of the trapezoid. The maximum angular error one can make by assuming the trapezoid is symmetric with respect to the trajectory is

$$\alpha_{max} = \tan\left(\frac{\delta_1 + \delta_2}{2R}\right)$$

$$\approx \frac{\ell \sin\theta}{2S}\left(\cos\theta + \frac{2x}{R}\right)$$

In this experiment

$$S = 120 \text{ in.}$$

$$\ell = 5 \text{ in.}$$

$$R = 1 - 4 \text{ in.}$$

$$X = 0 - 5 \text{ in.}$$

Averaging over θ, X, and R we obtain a typical $\alpha_{max} = 2.2$ deg corresponding to an RMS error of 1.2 deg.

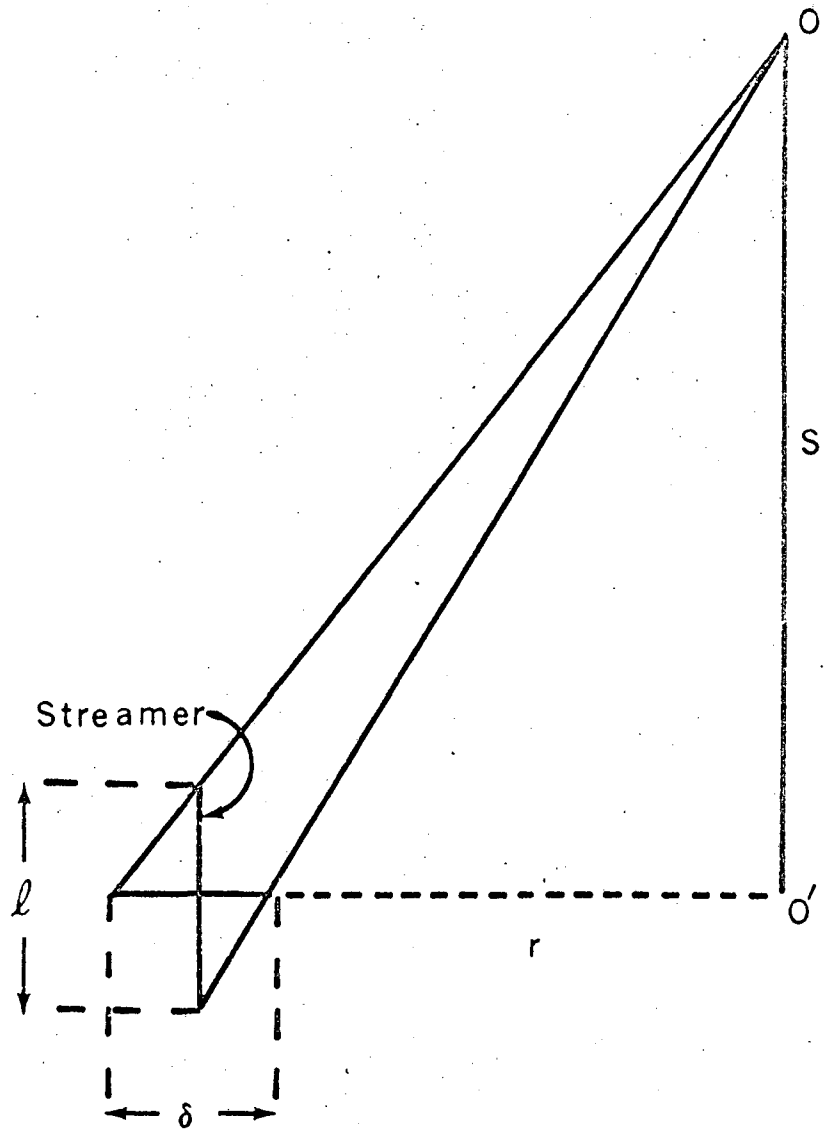

XBL 688-5650

Fig. 21. Coordinate system used to calculate the apparent broadening of a streamer which is situated at a point off the optical axis.

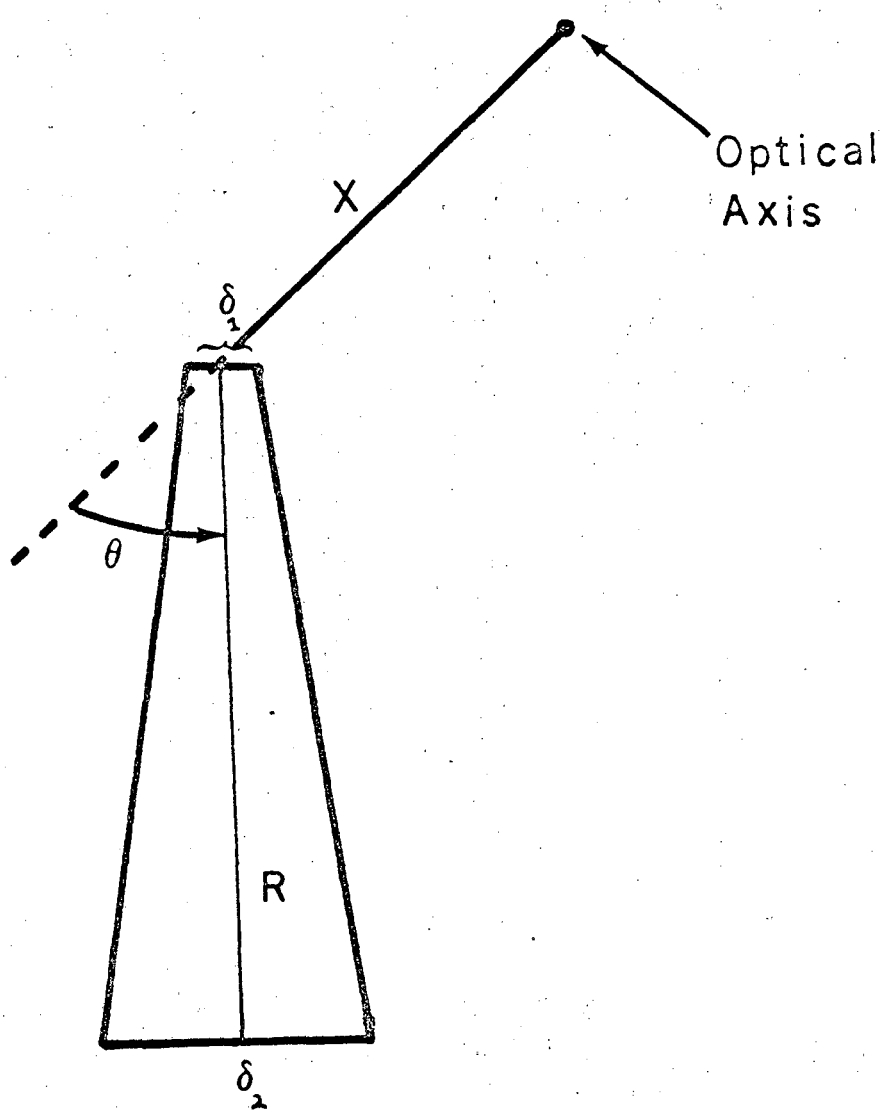

XBL 688-5651

Fig. 22. The trapezoid represents a broad tract located off the optical axis. This diagram defines the coordinates X, θ , and R which are used in the calculations in Appendix C. 1.

2. Propagation of Errors

Care must be taken in estimating the uncertainty in the c.m. angle θ due to errors in the projected proton and alpha scattering angles θ_1^P and θ_2^P since these errors propagate in two independent ways; i.e., our knowledge of the actual scattering angle θ_1 is not only limited directly by the uncertainty in θ_1^P but also by the uncertainty in the azimuthal angle ϕ which in turn depends on θ_1^P and θ_2^P.

Since the original and projected polar angles are related by

$$\tan \theta_1^P = \cos \phi \tan \theta_1$$

$$\tan \theta_2^P = \cos \phi \tan \theta_2$$

we can define the ratio R

$$R = \frac{\tan \theta_2^P}{\tan \theta_1^P} = \frac{\tan \theta_2}{\tan \theta_1}$$

which is independent of ϕ. It can be shown that for non-relativistic elastic scattering

$$\cos \theta = \frac{R - \beta}{R + 1}$$

where $\beta = M_1/M_2 \approx 1/4$. Now

$$\frac{\partial \theta}{\partial \theta_i^P} = \left[\frac{d \cos \theta}{d \theta} \right]^{-1} \frac{d \cos \theta}{dR} \frac{\partial R}{\partial \theta_i^P} \quad i = 1, 2$$

all three factors can be evaluated by straightforward differentiation. The standard error on θ is then

$$\delta\theta = \sqrt{\sum_{i=1}^{2} \left(\frac{\partial \theta}{\partial \theta_i^P} \delta\theta_i^P \right)^2} .$$

$\delta\theta$ is plotted as a function of θ in Fig. 23 for $\delta\theta_1^P$ = **.59 deg** and $\delta\theta_2^P$ = **1.45 deg.**

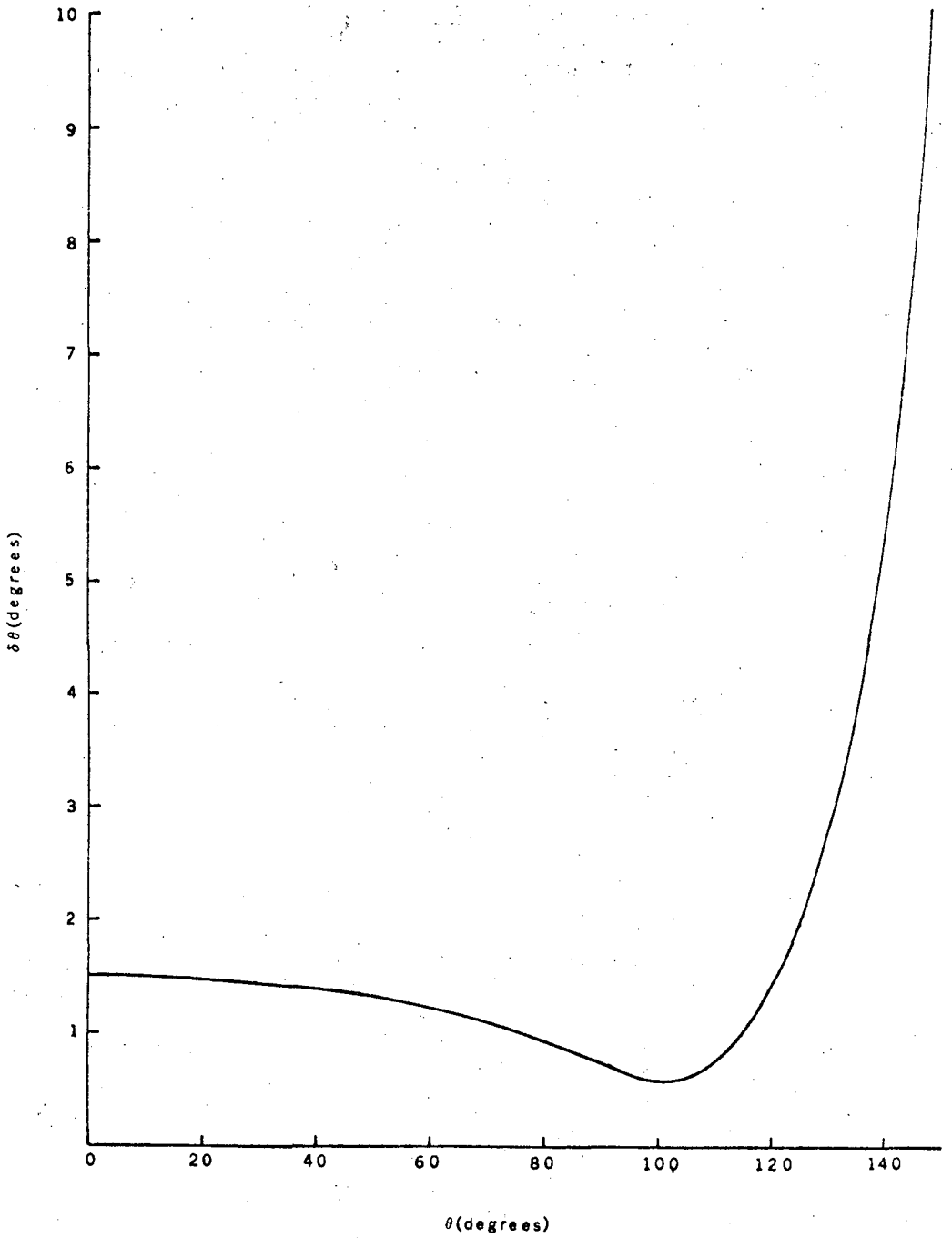

XBL 688-5045

Fig. 23. Uncertainty in the c.m. angle due to the errors $\delta\theta_1^p$ = 0.59 deg and $\delta\theta_2^p$ = 1.45 deg in the measured scattering angles.

D. Statistical Accuracy of Polarization Data

In the notation of Appendix B, the relation among asymmetry, analyzing power, and beam polarization is

$$P_0 P(\theta) = a_\theta$$

(We are ignoring the small azimuthal acceptance ϕ_0.) Suppose there are N events with angle θ. As an unbiased estimater for $P(\theta)$ take

$$P^*(\theta) = \frac{1}{NP_0} \sum_{i=1}^{N} \epsilon_i$$

where $\epsilon_i = \pm 1$ depending on whether the particle scattered left or right. The variance of P^*

$$V(P^*) = \left(\frac{1}{NP_0} \right)^2 N\, V(\epsilon_i)$$

$$= \frac{1}{NP_0^2} \left[\langle \epsilon_i^2 \rangle - \langle \epsilon_i \rangle^2 \right]$$

or, the standard error

$$\sigma(P) = \frac{1}{P_0} \sqrt{\frac{1 - a_\theta^2}{N}}$$

LEGAL NOTICE

This report was prepared as an account of Government sponsored work. Neither the United States, nor the Commission, nor any person acting on behalf of the Commission:

A. Makes any warranty or representation, expressed or implied, with respect to the accuracy, completeness, or usefulness of the information contained in this report, or that the use of any information, apparatus, method, or process disclosed in this report may not infringe privately owned rights; or

B. Assumes any liabilities with respect to the use of, or for damages resulting from the use of any information, apparatus, method, or process disclosed in this report.

As used in the above, "person acting on behalf of the Commission" includes any employee or contractor of the Commission, or employee of such contractor, to the extent that such employee or contractor of the Commission, or employee of such contractor prepares, disseminates, or provides access to, any information pursuant to his employment or contract with the Commission, or his employment with such contractor.

TECHNICAL INFORMATION DIVISION
LAWRENCE RADIATION LABORATORY
UNIVERSITY OF CALIFORNIA
BERKELEY, CALIFORNIA 94720